Journal Pre-proof

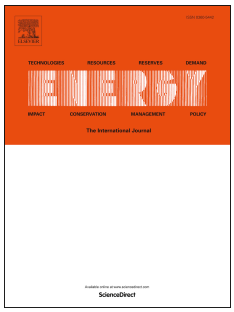

Low-speed, low induction multi-blade rotor for energy efficient small wind turbines

Oktay Yilmaz

PII: S0360-5442(23)02001-7

DOI: https://doi.org/10.1016/j.energy.2023.128607

Reference: EGY 128607

To appear in: *Energy*

Received Date: 15 March 2023

Revised Date: 26 July 2023

Accepted Date: 30 July 2023

Please cite this article as: Yilmaz O, Low-speed, low induction multi-blade rotor for energy efficient small wind turbines, *Energy* (2023), doi: https://doi.org/10.1016/j.energy.2023.128607.

This is a PDF file of an article that has undergone enhancements after acceptance, such as the addition of a cover page and metadata, and formatting for readability, but it is not yet the definitive version of record. This version will undergo additional copyediting, typesetting and review before it is published in its final form, but we are providing this version to give early visibility of the article. Please note that, during the production process, errors may be discovered which could affect the content, and all legal disclaimers that apply to the journal pertain.

© 2023 Published by Elsevier Ltd.

This manuscript version is made available under the CC-BY-NC-ND 4.0 license

https://creativecommons.org/licenses/by-nc-nd/4.0/

Journal Pre-proof

CRediT author statement

Oktay Yilmaz: Conceptualization; Data curation; Formal analysis; Investigation; Methodology; Resources; Software; Validation; Visualization; Roles/Writing - original draft; Writing - review & editing.

Journal Pre-proof

Journal Pre-proof

Low-speed, low induction multi-blade rotor for energy efficient small wind turbines

Oktay Yilmaz *

Faculty of Naval Architecture and Maritime, Marine Engineering Department, Yildiz Technical University, Yildiz Campus, Besiktas, Istanbul 34349, Turkey

Journal Pre-proof

* Corresponding author:
Faculty of Naval Architecture and Maritime, Marine Engineering Department, Yildiz Technical University, Yildiz Campus, Block-T, 1st Floor, 34349 Besiktas, Istanbul, Turkey.

E-mail address: oktay@yildiz.edu.tr

Abstract

To promote the deployment of small wind turbines (SWTs), thorough understanding of design parameter implications is essential. In-depth research is required to comprehend the influence of design TSR on off-design wind speed performance of multi-blade SWTs. In-house built blade element momentum algorithm was employed, which considered Reynolds number dependence of aerodynamic coefficients and correlated well with experimental results. Peak power coefficients were produced for 0.9, 1.5, 2 and 3 m diameter S826 rotors with blade numbers from 2 to 12 and design TSR of 2 to 10. Remarkably, regardless of diameter, greatest $C_{P,max}$ values were achieved around design TSR of 4. For peak efficiency, smaller the diameter, narrower the blade number and design TSR range. High-speed rotors have wider TSR range for high power coefficient. Yet, it was shown that operating TSR of low-speed rotors deviates less from design TSR as wind speed varies. It was revealed that low-speed (with a threshold design TSR of 3), low-induction multi-blade rotors provide high $C_{P,max}$, better efficiency at off-design, shorter starting time and lower wind speed than three-bladed high-speed rotor. A small boost in operational TSR was found to effectively mitigate loss in off-design performance. These are key features to maximize energy harvesting.

Keywords: Low induction rotor, Glauert optimum rotor, design tip speed ratio, blade number, off-design performance, starting capability

1 Introduction

Increasing the use of renewable energy in electricity generation is crucial for decarbonizing energy production, reducing dependency on fossil fuels, and producing energy with national resources. In 2021, a total of 94 GW wind turbines was installed worldwide, and the wind power plant capacity increased to 837 GW [1]. In 2020, renewable energy (solar, hydraulic, and bioenergy led by wind) met 19.6% of Germany's total energy needs and 45.3% of its electricity consumption [2]. Nevertheless, 2022 has been designated as the year with the highest global greenhouse gas emissions. According to the Paris Agreement, global average temperature increase should be limited to 1.5 ^{o}C to mitigate the effects of climate change. The transition to wind energy must be accelerated over the next decade for the world to become carbon neutral by 2050 [1]. In this regard, efficiency-enhancing approaches in wind energy technology are undoubtedly essential.

The IEC 61400-2 standard defines SWTs as having a rotor swept area of less than 200 m^2, corresponding to roughly 50 kW rated power generated at a voltage less than 1000 Vac or 1500 Vdc [3]. SWTs are utilized for the electricity needs of individual homes, rural schools, clinics, city buildings, industrial facilities, and university campuses. SWTs find application in city lighting, small appliance charging, energy support for fishing boats and yachts, pumping, fresh water production, hybrid renewable energy systems, energy storage, remote monitoring, research, and telecommunication stations [4,5]. SWTs become more appealing due to factors such as their suitability for individual investment, environmental concerns, and the option to sell excess electricity

to the grid, depending on the country's legislative framework [6]. Grid connection is more suitable for larger sized SWTs due to the added costs of local zoning, permits, and utility connectivity [7]. The energy costs of SWTs are constantly decreasing because of improvements in turbine efficiency and manufacturing processes [8].

SWTs with a rated power of 1-5 kW operate with blade Reynolds numbers less than 5×10^5 [9], whereas large wind turbines (LWTs) in the MW scale from 4×10^6 to 10^7 [10]. As a result, their aerodynamic efficiency is lower than LWTs [3]. LWTs typically feature three-bladed rotors with a design tip speed ratio (TSR) ranging from 8 to 10. When designing SWT rotors with diameters of 1-2 m to operate at such high tip speeds, their efficiency suffers due to the lower blade Reynolds number [11]. On the other hand, the blade number in LWTs is restricted to three due to factors such as weight, cost, and structural strength. Multi-blade construction is allowed with SWTs due to lower blade costs and easier manufacture. Multi-blade rotors are known to be more efficient due to reduced tip losses [12].

SWTs typically operate in the lower atmospheric boundary layer, which is characterized by high turbulence and low wind speeds due to nearby obstacles [13]. SWTs frequently experience periods of stopping and restarting [14]. Most SWTs have fixed pitch blades for ease of operation and low maintenance cost [15]. The starting torque of SWTs is comparable to the drivetrain resistive torque due to the high blade attack angles [16]. These factors lead to higher starting wind speeds, longer starting times, and reduced operating times [17,18]. The energy costs of SWTs are relatively higher compared to MW-scale LWTs. Extending operational times and improving SWT aerodynamic efficiency would increase energy harvesting, reducing energy costs and payback times, thereby enhancing economic attractiveness [19,20].

Today, most small and large turbines work on the variable speed mode, allowing them to operate around the optimum TSR across a wide range of wind speeds, resulting in an increased energy harvest. While LWTs cannot keep up with fluctuations in wind speed due to their high rotational inertia, SWTs react rapidly to changes in wind speed due to their low inertia. Nevertheless, the rotor speed controlled by the maximum power point tracking (MPPT) algorithm may not precisely track the wind speed due to measurement delays, response time of the control system, and rotor inertia [19,21]. Therefore, SWTs operate over a wide range of TSR and blade attack angles [17]. To maximize energy capture, variable-speed turbines must maintain a high power coefficient in off-design conditions [22].

Singh and Ahmed [23] designed two-bladed, 1.26 m diameter rotor with AF300 coded blade for low wind regions. The rotor was made of wood for low inertia and produced the highest power output at 18° blade pitch during open field tests. Akour et al. [21] constructed a three-bladed, 1 m diameter BW3 rotor with a design TSR of 3.5. The peak power coefficient was 0.38 at TSR = 4.4. They suggested that rather than a single SWT

with diameters ranging from 5.5 to 9.2 m, a cluster of micro turbines with the same total rated power would generate more energy at lower costs. Torres-Madroñero et al. [6] also reported similar outcomes.

Vertical-axis wind turbines (VAWTs) should be mentioned while discussing lifetime energy harvest in SWTs. Despite being less efficient than horizontal-axis wind turbines (HAWTs), VAWTs have an important benefit in terms of omnidirectional wind capture [24]. VAWTs, on the other hand, have higher rotational inertia than HAWTs, which results in a longer response time to wind speed changes [25]. As a result, maintaining good off-design efficiency is also crucial for VAWTs to mitigate performance loss. Zhang et al. [26] achieved a 6.7% improvement in C_P at the design TSR and a 10% improvement in C_P at off-design TSR values for a 1.7 m diameter, 2-blade Darrieus VAWT with optimal twisted winglet design. The visualization demonstrated that the winglet effectively attenuated the intensity of the tip vortices. According to the results of the computational fluid dynamic (CFD) investigation, Zhang et al. [24] found that the 2 m diameter VAWT with a straight blade and symmetrical airfoil reached the highest power coefficient. Among the tested NACA profiles, NACA0018 was determined to be the optimal airfoil that maximized the power coefficient, while thinner profiles experienced early stall.

In recent years, there has been increased research on multi-bladed SWTs [27-31], which are suited for low-speed operation. They can provide high starting torque due to their large solidity and pitch angles. Low-speed multi-bladed SWTs are considerably quieter than high-speed 3-bladed SWTs of the same diameter, as noise is proportional to the fifth power of rotor RPM [32,33]. Dynamic rotor analyses indicated that five-bladed turbine outperformed three-bladed turbine in response to wind fluctuations, resulting in higher energy production [30]. In the commercial sector, there is also a growing preference for multi-bladed rotors, three of which appear in Table 1. The power coefficients of rotors shaped from low-efficiency airfoils are maximized at a lower design TSR [34]. Consequently, there has been an increase in research focusing on the design TSR as a design parameter [11,35].

Table 1. Three commercial multi-bladed wind turbines.

Model name	Rated power	Diameter	Blades	Starting (U_s) or cut-in (U_c) speed	Web page
Wind Scorpian	225 W at 8 m/s	1.5 m	11	U_s = 1.5 m/s	hydrogenappliances.com
Rutland 914i	260 W at 15 m/s	0.91 m	6	U_c = 3 m/s	marlec.co.uk
VEVOR	500 W at 13 m/s	1.19 m	5	U_s = 2 m/s	eur.vevor.com

It is worth mentioning here for low induction rotors (LIRs), which have recently focused on LWTs (offshore turbines with 10-15 MW in particular) [36-38]. The LIR, as the name suggests, is configured for an axial induction factor less than the optimum value of 1/3. LIRs demand lower structural strength. Energy costs can be reduced due to lower tower, rotor construction and material costs [39]. SWTs have not yet been examined

in the published literature under the designation of LIR. Since the axial induction factor is highly sensitive to blade pitch angle, studies investigating the impact of pitch angle on aerodynamic efficiency indirectly consider rotors with different degrees of induction (low or high) [40-43].

Table 2 outlines research on multi-bladed turbines from the past to the present. The aerodynamic performance of such turbines was assessed considering airfoil type [11,27], diffuser configuration [32], and yaw angle [40]. Cm scale micro turbines with high solidity (around 1) [44,45] and wind-water pumps designed for high torque rather than electricity production [40,46,47] were also addressed. Multi-bladed rotor studies based on energy efficiency have been performed in a limited range of blade number and design TSR [29,30,48]. The two comprehensive works were conducted by Wilson et al. [43] and Duquette et al. [49]. Wilson et al. [43] used the BEM theory to derive theoretically achievable $C_{P,max}$ values for various *L/D* ratios and blade numbers, independent of diameter and airfoil type. Duquette et al. [49], on the other hand, concentrated on finding the optimum solidity and blade number in the SG6043 rotors, with 3, 6 and 9 blades and $C_{P,max}$ being the main target. Revisited theoretical analyses have been conducted to illustrate the peak power coefficient based on design TSR for specific *L/D* ratios [34] and blade numbers [50]. The blade Reynolds number, and consequently, blade efficiency, are significantly influenced by the blade number and design TSR. Yilmaz [11] has recently worked on the strategy of determining the optimum design TSR and blade number for high power coefficient over a wide TSR range of S826 and SD7032 rotors. Given that recent research is being redirected to multi-bladed turbines, an in-depth reconsideration after years is needed. The effect of design TSR on aerodynamic efficiency at off-design tip speeds, particularly off-design wind speeds, still requires extensive investigation.

Table 2. (Continued) Multi-blade turbine research in the literature.

Research method	Rotor and test parameters	Objective, methodology, performance data and outcome	Reference
BEM theoretical analyses	B = 1, 2, 3, 4, ∞ λ_{dsg} = 4 to 24 L/D = 10 to 160, ∞	-Achievable $C_{P,max}$ depending on design TSR (λ_{dsg}) for a range of L/D and blade number (B) -The theoretical design strategy is well explained.	Wilson et al. [43]
BEM predictions	D = 4.65 m B = 48; λ_{dsg} = 1.75 Airfoil: Clark Y	-Bicycle wheel wind turbine ($C_{P,max} \cong 0.3$) -Deriving power curves depending on wind speeds at a constant RPM -Steep decrease in C_P above design wind speed (U_{dsg})	Wilson et al. [43]
Wind tunnel tests. BEM predictions	D = 0.5 m B = 3, 6, 12 U = 5 m/s	-Constant-chord, untwisted flat-plate blades -The highest $C_{P,max}$ for solidity (σ) = 0.2-0.3 and λ_{opt} = 2.5-3.5 -Effect of blade pitch (10°, 15° and 20°) on C_P-λ curve -The larger the blade pitch narrower the optimum TSR range	Duquette et al. [49]
Wind tunnel tests. BEM predictions	D = 0.5, 2 m B = 3, 6, 12 λ_{dsg} = 2 to 6 U = 6 to 8 m/s Airfoil: SG6043	-Solidity and blade number effects on $C_{P,max}$ -Glauert's optimum rotor design using fixed design C_l ($C_{l,dsg}$) -Increasing solidity leads to a higher $C_{P,max}$ in the λ range of 3-4. -$C_{P,max}$ = 0.52 for a 2 m diameter 12-blade rotor with λ_{dsg} = 3.75 and σ = 0.14.	Duquette et al. [49]
Open jet wind tunnel	D = 0.3 m B = 10; λ_{opt} = 2 σ = 32.5%	-Performance testing of a 1/8 scale model wind-water pump -Constant chord and twisted blades -The best pitch angle for the greatest $C_{P,max}$ (0.36) was 15°.	Sarkis and Pinilla [46]

Table 2. (Continued) Multi-blade turbine research in the literature.

Research method	Rotor and test parameters	Objective, methodology, performance data and outcome	Reference
Open field tests. BEM predictions	D = 1.3 to 4.4 m B = 9, 12; λ_{dsg} = 2 U_{test} = 11 m/s	-Power performance testing of ducted multi-blade turbine -Reduced noise with low-speed rotor -$C_{P,avg}$ ranged from about 0.55 to 0.8.	Visser [32]
BEM predictions	D = 3 m B = 5; λ_{dsg} = 2, 4, 6 U = 11 m/s Airfoils: NACA4421 flat plate, SG6043	-Guidance on airfoil selection -Glauert optimum rotor design -Comparison of C_P-λ curves -Low L/D ratio flat plate reached the $C_{P,max}$ with low λ_{dsg}, and the high L/D ratio SG6043 with high λ_{dsg}.	Kanya and Visser [27]
BEM theoretical analyses	B = ∞, λ_{dsg} = 1 to 10 L/D = 25 to 200, ∞	-Deriving the achievable $C_{P,max}$ depending on L/D ratio and λ_{dsg}	Pinho and Gonçalves [34]
Open field tests. BEM prediction	D = 3.4 m, B = 9 λ_{dsg} = 3.2 U_{dsg} = 10 m/s Airfoil: Eppler 197	-Glauert optimum rotor design -$C_{P,overall}$ = 0.3 (including generator, gearbox and inverter efficiency) -Power loss was minimal up to 20°-30° yaw angle.	Sant et al. [40]
Open test section in wind tunnel. RANS CFD	D = 2 m B = 2, 3, 5, 6 U_{test} = 6, 7, 8 m/s	-The effect of B on flow field, C_P, C_T and C_Q for varying TSR -Rotors were configured by removing or adding a blade to the baseline 3-bladed rotor. -The 3-bladed rotor was 2-4% more efficient than the 5- and 6-bladed rotors.	Eltayesh et al. [29]
Dynamic BEM analyses	D = 2 m B = 3, 5 U_{test} = 3 to 10 m/s TI = 0.3 to 0.6 Airfoil: SD7062	-Three-bladed rotors were optimized for reduced starting time, while the 5-bladed rotor was adapted from the 3-bladed best C_P rotor. -The 5-bladed rotor produced 25% more power from turbulent wind at low wind speeds.	Porto et al. [30]
Wind tunnel tests	D = 2 m B = 3, 5 U = 4.5 to 11.5 m/s	-Dynamic rotor tests with oscillating wind speed. -The 3-bladed rotor achieved a slightly higher $C_{P,max}$ (0.435) than the 5 bladed rotor.	Vedovelli et al. [31]
Wind tunnel tests. LES-CFD analyses	D = 0.18 m B = 2, 3, 4, 5 U_{test} = 7 m/s Airfoil: NEFU6518	-The effects of B on wake characteristics -Rotors were configured using the base blade of the 3-bladed rotor. -Three-bladed rotor achieved greatest $C_{P,max}$ (0.37). -Lower velocity deficit in the 5-bladed rotor wake	Zhang et al. [48]
Wind tunnel tests	D = 0.2 m; B = 8 λ_{dsg} = 1; U = 15 m/s Airfoil: SG6042	-Glauert, Betz and Joukowsky rotor design approaches were compared based on flow field and power performance. -Glauert optimum rotor achieved the highest $C_{P,max}$ (0.34).	Bourhis et al. [51]
BEM predictions. RANS-CFD validation	D = 0.9 m B = 3, 4, 5, 6, 7 λ_{dsg} = 3, 4, 5, 6 U_{dsg} = 10 m/s Airfoil: S826 and SD7032	-Strategy to determine the proper λ_{dsg} and B to maximize $C_{P,max}$ and extend optimum TSR range with a limited number of trial BEM designs and performance analyses -Glauert optimum rotor design using fixed $C_{l,dsg}$ -The impact of axial induction factor and local blade AoA on the off-design TSR performance was addressed.	Yilmaz [11]

Journal Pre-proof

Table 2. Multi-blade turbine research in the literature.

Research method	Rotor and test parameters	Objective, methodology, performance data and outcome	Reference
Wind tunnel tests	D = 0.68 m B = 3, 6, 12, 24 λ_{opt} = 1-1.5 σ :on the order of 1 Circular-arc twisted, constant-chord blades	-To investigate torque and power characteristics of the wind-water pump. -Aerodynamic efficiency constantly increased with B. -$C_{P,max}$ of the 24-bladed was around 0.25. - High solidity rotors exhibited increased torque at low TSR due to blade interaction.	John et al. [47]
BEM predictions. BET starting estimations. RANS-CFD validation	D = 0.9, 1.5, 2, 3 m B = 2 to 12 λ_{dsg} = 2 to 12 U_{dsg} = 10 m/s Airfoil: S826	-Scanning the λ_{dsg}-B parameter space to gain a thorough understanding of rotor aerodynamic performance metrics -Glauert optimum rotor design -Adoption of $C_{l,dsg}$ matching the blade Re number -The effect of λ_{dsg} on optimum TSR and wind speed ranges -Multi-blade LIRs with low λ_{dsg} (not less than 3) outperformed the high-speed 3-blade rotor over practically the entire wind speed range. -Increased operating RPM of best C_P rotors offered a significantly less C_P reduction in off-design conditions.	Present study

This research has two primary objectives. The first is to examine how the design TSR and blade number affect rotor performance metrics such as $C_{P,max}$, $C_{T,opt}$, natural time constant, and blade Reynolds number. The second objective is to identify optimum *design TSR-blade number* combinations that maximize $C_{P,max}$, maintain high efficiency at off-design wind speeds, and minimize the starting wind speed and time to increase lifetime energy harvest. The BEM algorithm, considering Re number dependence of sectional blade efficiency, was verified using measurements from a 0.9 m diameter turbine tested at the Norwegian University of Science and Technology (NTNU). Scanning *the design TSR-blade number* design space produced peak power coefficient curve families for S826 rotors with 0.9, 1.5, 2 and 3 m diameter. It was shown with reasoning how the low induction rotor, which has received no direct interest for SWTs, provides high aerodynamic efficiency across wide TSR and wind speed ranges.

2 Method

2.1 Performance validation of a 0.9 m diameter small wind turbine

2.1.1 BEM algorithm for rotor performance analysis

The BEM methodology implemented in this work employed the Viterna-Corrigan post-stall model [52] to produce aerodynamic coefficients for high angles of attack (AoAs) (from 20° to 90°) experienced at low TSR. Buhl's [53] method was adopted for determining the axial induction factor in the wake state. Tip losses were considered with the Prandtl method. The BEM code used a combination of Methods 1 and 2 from Manwell et al.'s [12] book, page 125.

Figure 1 depicts the velocity triangle, design, and operating parameters at a blade section. Ω, U_{rel}, and U represent the rotor angular speed, relative and free stream wind velocity, respectively, while a and a' denote

the axial and rotational induction factors. φ, α ve θ indicate the relative wind angle, local AoA, and sectional pitch angle, respectively. The input parameters include *U*, λ, *R*, *B*, blade chord (*c*) and θ distribution. Tabulated airfoil lift and drag data for a range of Reynolds numbers are imported.

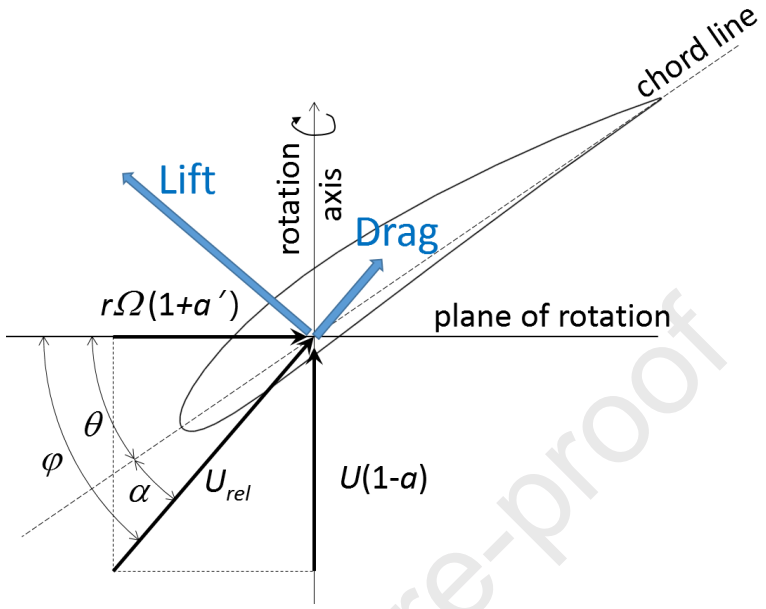

Fig. 1. Design, flow and operational parameters of a blade element.

Method 1 (a < 0.4)

1. The initial values of φ are specified by $\varphi_{initial} = (2/3)\arctan(1/\lambda_r)$, where $\lambda_r = \Omega r/U$. $Re = \Omega R c_{tip}/\nu$ is used to set the starting value of Re number.

2. The following equation for the lift coefficient arises from the derivation procedure of BEM equations (page 125 in Ref. [12]).

$$C_l = 4F\sin\varphi\frac{\cos\varphi - \lambda_r\sin\varphi}{\sigma_{local}\left(\sin\varphi + \lambda_r\cos\varphi\right)} \tag{1}$$

Where local solidity, $\sigma_{local} = Bc/2\pi r$. *F* is for the Prandtl's tip-loss factor.

$$F = \frac{2}{\pi}\cos^{-1}\left|\exp\left(-\frac{B}{2\sin\varphi}\left(\frac{R}{r}-1\right)\right)\right| \tag{2}$$

Intersecting point φ between the airfoil lift curve (see equation 3 and Fig. 4b) and equation (1) is determined using the bisection root finding method. φ is scanned from 0° to 90°.

$$C_l = \text{function of}\left(\alpha, \text{Re}\right) \quad \text{where } \alpha = \varphi - \theta \tag{3}$$

The blade was divided into *N* = 25 blade elements [54]. Typically, the solution starts with the first element at the blade root. For cases where the α value is close to the stall angle, if multiple roots exist, the solution starts from an intermediate blade element with a single root and progresses first towards the blade root and then towards the tip. When multiple roots present in a blade element near the blade tip, the solution progresses to ensure φ continuity between the blade elements.

3. Induction factors *a* and *a'* are determined.

$$a = \left(1 + \frac{4F \sin^2 \varphi}{\sigma_{local} C_l \cos \varphi} \right)^{-1} \tag{4}$$

$$a' = \frac{1}{2}\left(\sqrt{1 + \frac{4}{\lambda_r^2} a(1-a)} - 1 \right) \tag{5}$$

The relation proposed by Lanzafame and Messina [55] for *a'* was preferred instead of the commonly used expression similar to the one in equation (4).

4. After determining the local Re number, which varies with the radial position on the blade span ($Re = U_{rel} c/\nu$, where $U_{rel} = U(1-a)/sin\varphi$), the solution procedure returns to step 2. Iteration continues until φ reaches convergence.

5. When *a* is less than 0.4 in all blade elements, C_P is calculated using Method 1. This is the case with low λ.

$$C_P(\lambda) = \frac{8}{\lambda^2} \int_{\lambda_{root}}^{\lambda} F \lambda_r^3 a'(1-a)\left[1 - \left(C_d / C_l \right) \cot \varphi \right] d\lambda_r \tag{6}$$

To determine C_l and C_d, bilinear interpolation was applied to consecutive AoA and Re number values (Fig. 2a). Figures 2b-d depict how the lift and drag coefficients of the S826 profile change with Re number. Below Re = 10^5, the aerodynamic coefficients, particularly C_d, exhibit non-linear variation. As a result, spline interpolation may be preferable locally. However, considering the erratic variability of the experimental data (Fig. 2c), and to avoid complicating the interpolation procedure, linear interpolation on the Re number was preferred, as is employed in the literature [27]. Method 2 is used to continue the solution from the blade element where *a* exceeds 0.4.

Method 2 (a > 0.4, wake state)

1. Initial values of 0.5 and 0 are assigned to *a* and *a'*, respectively.

2. φ is determined using the equation derived from the velocity triangle (Fig. 1).

$$\varphi = \arctan\left(\frac{1-a}{(1+a')\lambda_r} \right) \tag{7}$$

The α, Re, F, C_l and C_d values are updated. The local thrust coefficient is calculated using the relation derived from the BEM theory (page 131 in Ref. [12]).

$$C_{T_r} = \frac{\sigma_{local}\left(1-a\right)^2\left(C_l\cos\varphi + C_d\sin\varphi\right)}{\sin^2\varphi} \tag{8}$$

3. A is updated using Buhl's wake state model, incorporating an underrelaxation factor (w) of 0.5.

$$a_{new} = \left(1-w\right)a + w\frac{18F - 20 - 3\sqrt{C_{T_r}\left(50-36F\right)+12F\left(3F-4\right)}}{36F-50} \tag{9}$$

The equation (5) is used to update a' before returning to the second step. Once a reaches convergence, C_P is calculated using equation (6). Implementing Methods 1 and 2 in this manner successfully prevented numerical instability that may occur around the stall AoA and in the wake state [57]. The BEM algorithm was built using the MATLAB software.

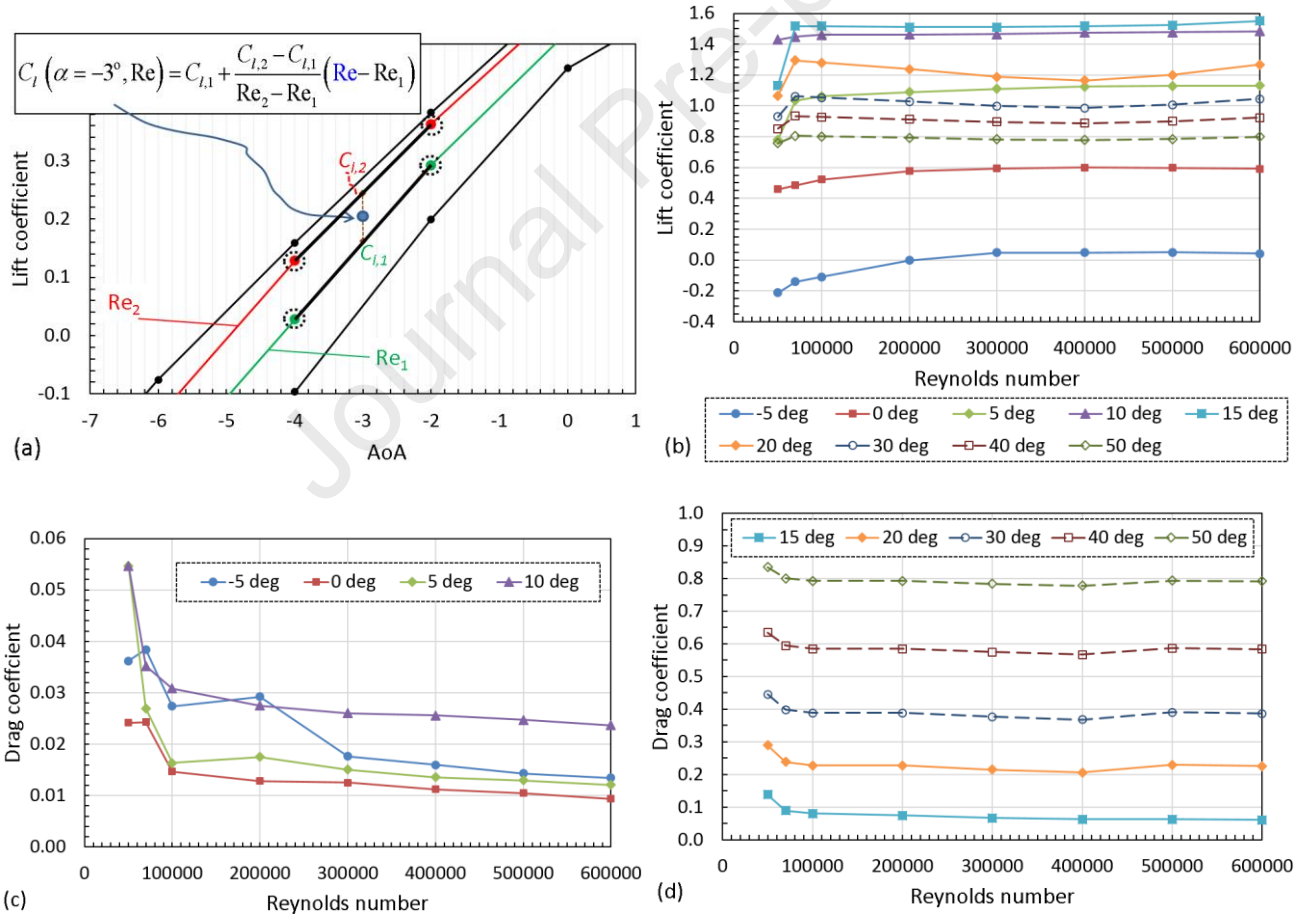

Fig. 2. (a) Illustration of bilinear interpolation on AoA and Re number. Variation of experimental (b) lift and (c, d) drag coefficients [56] of S826 depending on Reynolds number for various fixed AoA values (continuous lines). It should be mentioned that C_l and C_d values above AoA of 20° were predicted by Viterna-Corrigan post-stall model (dashed lines).

2.1.2 Comparison of BEM predictions with experimental and CFD results

The performance tests of a 0.9 m diameter, 3-bladed turbine in a closed wind tunnel at NTNU were used to validate the BEM algorithm (Fig. 3). The blades of the Reference Rotor were shaped with S826 airfoil. The *design* wind speed and TSR were 10 m/s and 6, respectively. Krogstad and Lund's [58] publication includes experimental details as well as a complete description of the Reference Rotor. S826 profile was developed by the National Renewable Energy Laboratory (NREL), USA, for variable-speed turbines with a diameter of 20-40 m [59]. Because of its high aerodynamic efficiency above Re = 100,000, it also performs well for SWTs several meters in diameter. The experimental aerodynamic coefficients of S826 published by Bartl et al. [56] were incorporated into the BEM algorithm (Fig. 4). In wind tunnel experiments, the blockage ratio was 11.8%. Figure 5 presents the experimental data with Glauert blockage correction applied [60]. The figure also includes results from two SST k-ω RANS-CFD simulations, one with the turbine pole [61] and the other without. The turbine pole has a noticeable effect around the optimum TSR, as indicated by the CFD results [62]. In comparison to the CFD and experiment, BEM approximates $C_{P,max}$ with a relative error of 1.6% and 2.9%, respectively, and the BEM's average relative error values over the whole TSR range are 7.6% and 8.3%. The range of λ = 3-4, with local AoA varying between 10° and 20°, shows the most evident deviation from the experimental data, encompassing the dynamic stall development and transition to full stall [55]. This challenge impairs the accuracy of aerodynamic force estimation by BEM, a semi-empirical modeling method. In the Viterna-Corrigan model [52], significant overprediction of C_P at low λ occurred when using stall AoA as the starting angle for post-stall aerodynamic coefficient generation. In this study, a starting angle of 20° post-stall angle was employed which improved BEM prediction [63].

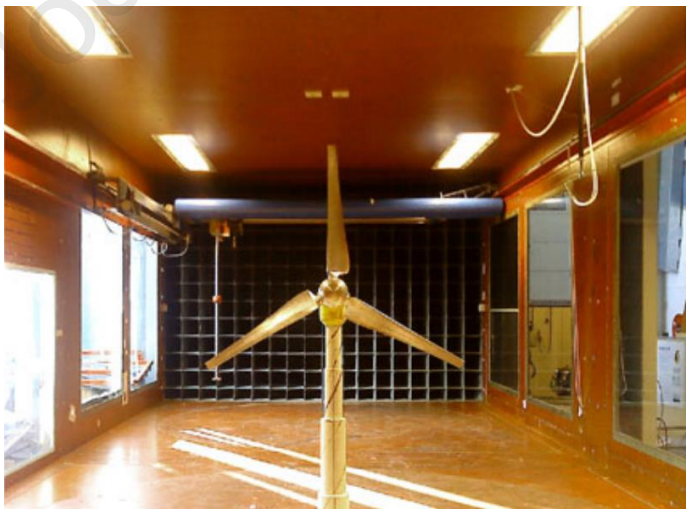

Fig. 3. The Reference Rotor in closed wind tunnel at the NTNU [58].

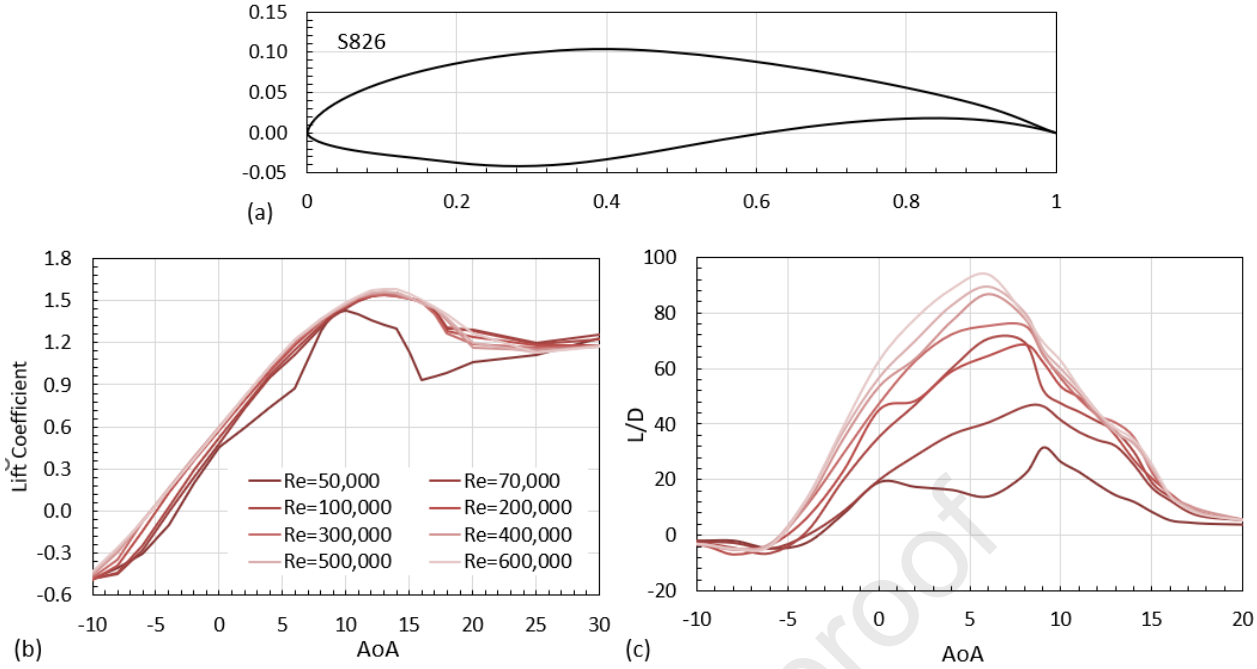

Fig. 4. (a) S826 airfoil. Reynolds number dependent experimental (b) lift coefficient, and (c) *L*/*D* ratio [56].

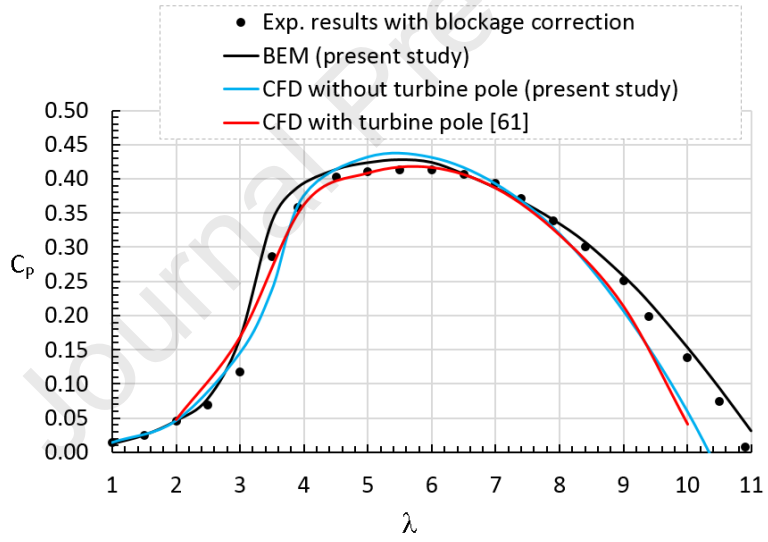

Fig. 5. Comparison of the BEM predictions with experimental [58] and CFD results.

2.2 Rotor design

For blade chord and pitch distribution, Glauert optimum rotor design equations (equations 10-12) were employed (Manwell et al.'s [12] book, page 132). In the genetic optimization algorithm, scanning a wide design space of pitch angle and chord, the best C_P rotor converges to the Glauert optimum [3,64]. The design equations are derived by accounting for wake rotation, while ignoring blade drag and hub-tip losses. Considering drag in the design has a negligible effect on the pitch and chord distribution [34]. The relative wind angle is determined by,

$$\varphi = \frac{2}{3}\arctan\left(\frac{1}{\lambda_r}\right) \tag{10}$$

Here, λ_r (=$\lambda_{dsg}\, r/R$) is the local speed ratio. λ_{dsg} (=$\Omega R/U$) refer to the design TSR. The chord and pitch angle are given by,

$$c = \frac{8\pi r}{BC_{l,dsg}}\left(1-\cos\varphi\right) \tag{11}$$

$$\theta = \varphi - \alpha_{dsg} \tag{12}$$

The *L/D* ratio of the S826 airfoil reaches its maximum at around 6° for most Re numbers. Although the airfoil efficiency peaks at larger angles for low Re, the design AoA (α_{dsg}) was adopted as 6° in all rotor designs to avoid early stalling at low λ.

Verma and Baloni [65] underlined the importance of considering the operational Reynolds number in BEM method. Ignoring the effect of Re number can result in inefficient rotor designs and inaccurate performance predictions. Therefore, $C_{l,dsg}$ was determined iteratively to match the tip Re number (Fig. 6), where $Re_{tip} = U_{rel}c_{tip}/\nu$ and $U_{rel} = U(1-a)/\sin\varphi$. The following equation is used to determine the axial induction factor corresponding to the peak efficiency of the Glauert optimum rotor (Ref. [12], page 132).

$$a = \left(1+\frac{4\sin^2\left(\varphi\right)}{\sigma_{local}C_{l,dsg}\cos\left(\varphi\right)}\right)^{-1} \tag{13}$$

In this study, $C_{l,dsg}$ ranged from 0.872 to 1.221, depending on the Re_{tip}. $C_{l,dsg}$ value was fixed across the blade span due to the nearly constant Re number for the majority of the blade [9].

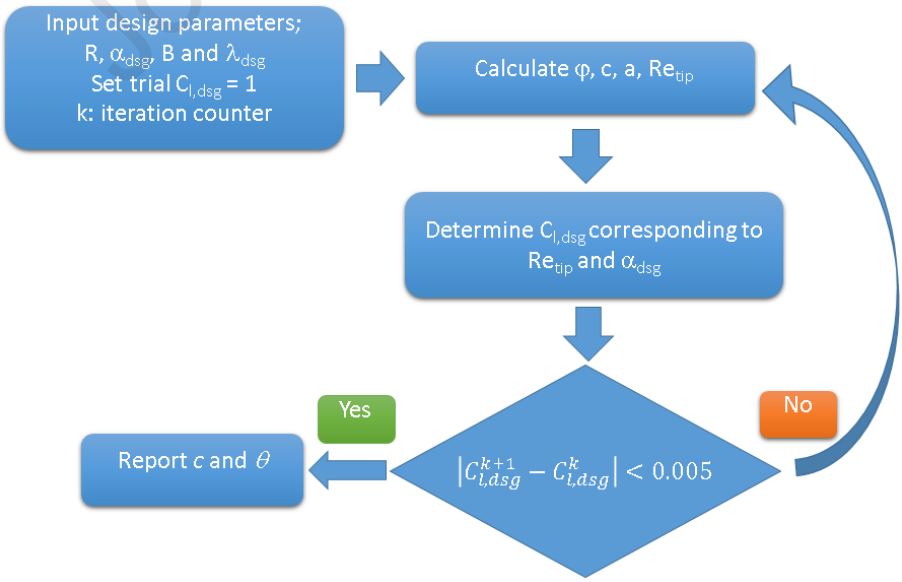

Fig. 6. Iteration procedure for matching the Re_{tip} and $C_{l,dsg}$.

Considering the startup time, it seems necessary to make the blades hollow to reduce inertia. However, due to small size, challenges arise in bonding the pressure and suction surfaces and achieving the correct blade profile. Solid high-density resin-fiberglass composite blades have a relatively large rotor inertia. Solid low-density timber blades are attractive in this regard. Biomaterial blades would be a better choice for environmentally friendly wind turbines than petroleum-derived resin blades [3].

Peterson and Clausen [66] tested hoop pine rotor blades for a 2 m diameter, 600 W rated turbine and found unlimited fatigue strength up to a wind speed of 20 m/s, making it suitable for 1 m long blades [33]. Based on these considerations, rotor design parameters are summarized in Table 3.

Considering hub-tip losses leads to shorter chord at the blade ends [19], reducing inertia and noise while sacrificing some efficiency [67]. Given the broad λ_{dsg}-B parameter space searched for, the Glauert optimum rotor design was adopted to investigate the influence of these variables on aerodynamic efficiency. Once a suitable λ_{dsg}-B combination is determined, deviations from the best C_P rotor geometry for different purposes can be considered before manufacturing.

Table 3. Input rotor design parameters.

Parameter and value	**Parameter and value**	**Parameter and value**
D = 0.9, 1.5, 2 and 3 m	U_{dsg} = 10 m/s	Starting TSR, λ_s = 1
$D_{hub} = 0.1D$	P_{rated} = 150, 400, 700, 1500 W	Blade profile: S826
α_{dsg} = 6°	Q_r = 0.04, 0.17, 0.34, 0.76 Nm	Blade material: hoop pine
B = 2, 3,…,12	ρ_b = 550 kg/m^3; ρ_{air} = 1.2 kg/m^3	Blade type: solid
λ_{dsg} = 2, 3,…,10		

2.3 Starting performance predictions

The blade element theory (BET) method was used for starting performance predictions. The BET predictions showed reasonable agreement with start-up tests conducted on SWTs in the literature [3,17]. Once the rotor RPM reaches a predetermined speed, electricity production begins with the counter-torque generation in the generator [68]. The start-up sequence can be divided into two parts: idling and rapid acceleration. Poor acceleration is typical during the starting sequence because the blade attack angles are above 20° during the idling phase, which accounts for the majority of the sequence. As a result, λ = 1, where the idling phase normally terminates [20,68], was considered as the end of the starting period.

During start-up, the wind accelerates the rotor rather than producing electricity in the generator. During this period, the rotor's impact on wind deceleration is minimal, hence axial and rotational induction factors are

disregarded [68]. The following is the relationship between angular acceleration, aerodynamic torque (Q), drivetrain resistive torque (Q_r) and rotational inertia (J).

$$\frac{d\Omega}{dt} = \frac{Q - Q_r}{J} \tag{14}$$

J is the sum of the rotor and generator rotational inertia. The generator inertia was not taken into account due to its relatively small magnitude. The blades account for the majority of rotor inertia [19,20].

$$J = B \int_{blade} r^2 dm = B \int_{r_{root}}^{R} r^2 \rho_b A dr \tag{15}$$

Here, ρ_b is the blade density, and A is the radially varying airfoil cross-sectional area. A = 837.16 mm^2 for S826 with 100 mm chord. Since the turbine was considered to be driven at variable speed by a permanent magnet generator, Q_r is equal to the generator cogging torque [35]. Generator cogging torques are provided in Wood's [3] book, page 21, against the rated power of commercial SWTs. The investigated rotors with diameters of 0.9 and 1.5 m have rated powers of 150 W and 400 W, respectively, at 10 m/s rated wind speed. The corresponding Q_r values were determined by interpolation as 0.04 and 0.17 Nm, respectively. With additional blades, an increase in radial load may lead to higher resistive torque in the bearings [16]. However, the selected timber density is lower (around half to one-third) than commonly used blade materials [33]. As the blade number increases, the structural load per blade decreases, making it favorable to choose efficient and thinner airfoils like BW3 to reduce blade mass [52].

In the BET method, aerodynamic torque is determined by,

$$Q = B \frac{1}{2} \rho_{air} \int_{r_{root}}^{R} \left(C_l \sin\varphi - C_d \cos\varphi \right) c W^2 r dr \tag{16}$$

$\varphi = arctan(U/\Omega r)$ in the absence of a and a'. The relative wind velocity is calculated as follows.

$$W = \sqrt{U^2 + \left(\Omega r\right)^2} \tag{17}$$

Equation (14) was numerically integrated with the 4th order Runge-Kutta method to obtain the angular speed change over time [69].

$$\Omega^{n+1} = \Omega^n + \frac{\Delta t}{6}\left(k_1 + 2k_2 + 2k_3 + k_4\right) \tag{18}$$

$$k_1 = g\left(t^n, \Omega^n\right) \tag{19a}$$

$$k_2 = g\left(t^n + \frac{\Delta t}{2}, \Omega^n + \Delta t \frac{k_1}{2}\right) \tag{19b}$$

$$k_3 = g\left(t^n + \frac{\Delta t}{2}, \Omega^n + \Delta t \frac{k_2}{2}\right) \tag{19c}$$

$$k_4 = g\left(t^n + \frac{\Delta t}{2}, \Omega^n + \Delta t k_3 \right) \tag{19d}$$

Where *n* refers to the time step index. The function *g* is the time rate of change of Ω,

$$g\left(t,\Omega\right) = \frac{d\Omega}{dt} = \frac{Q\left(t,\Omega\right) - Q_r}{J} \tag{20}$$

BET algorithm was implemented in MATLAB environment. A user-defined function was introduced for the repeated calculation of aerodynamic torque in equation (20). The procedure is outlined below.

1. Rotor parameters (B, R, J, Q_r), wind speed, time step (Δt), blade pitch and chord distributions are specified. The aerodynamic coefficient database is imported. Initial values of Ω and t are set as zero.
2. The spanwise distributions of W, Re, φ, α, C_l ve C_d are determined. The starting torque ($Q_{\lambda=0}$) is calculated. If $Q_{\lambda=0} < Q_r$, the turbine is unable to initiate rotation, and the calculation is terminated.
3. The angular speed at the next time step (Ω^{n+1}) is calculated. The calculation continues until the rotor reaches $\lambda = 1$.

2.4 Computational fluid dynamics simulations

Section 3.3 presents CFD results of 2-, 4-, and 6-bladed rotors to assess the BEM predictions. The Reynolds-averaged Navier-Stokes (RANS) turbulence modeling was employed to predict the flow around the rotor using ANSYS FLUENT 2021 software, which is a finite volume-based method. The centrifugal and Coriolis forces induced by the rotating rotor are included in the modified momentum equation using the Moving Reference Frame (MRF) approach. The MRF method reduces computational expense because it allows the problem to be handled independently of time [70,71]. The pressure-based continuity and momentum equations were solved simultaneously using the coupled solver. The governing differential equations, which include the pressure, velocity components, and turbulence variables, were discretized with second-order accuracy. The cell-centered and upwind schemes were employed to discretize the diffusion and convective terms, respectively. The least-squares cell-based method was utilized to calculate the gradients of variables.

The periodic boundary conditions were applied (Fig. 7) [29]. The computational domain extends up to a radius of 20R, with the rotor located at distances of 20R and 40R from the inlet and outlet, respectively. The blockage ratio, determined based on the rotor's swept area, is as low as 0.25%. The MRF region is 1.2R in diameter and 0.5R in width (Fig. 7e). The inlet boundary was set with a free-stream velocity of 10 m/s and a turbulence intensity of 0.3%, following the Reference Rotor experiments [58]. The far field boundary, located at a sufficient distance from the rotor to ensure negligible influence on flow variables, was modeled as a free-slip wall. The effective pressure at the outlet was specified as zero. The no-slip boundary condition was imposed on the turbine surfaces.

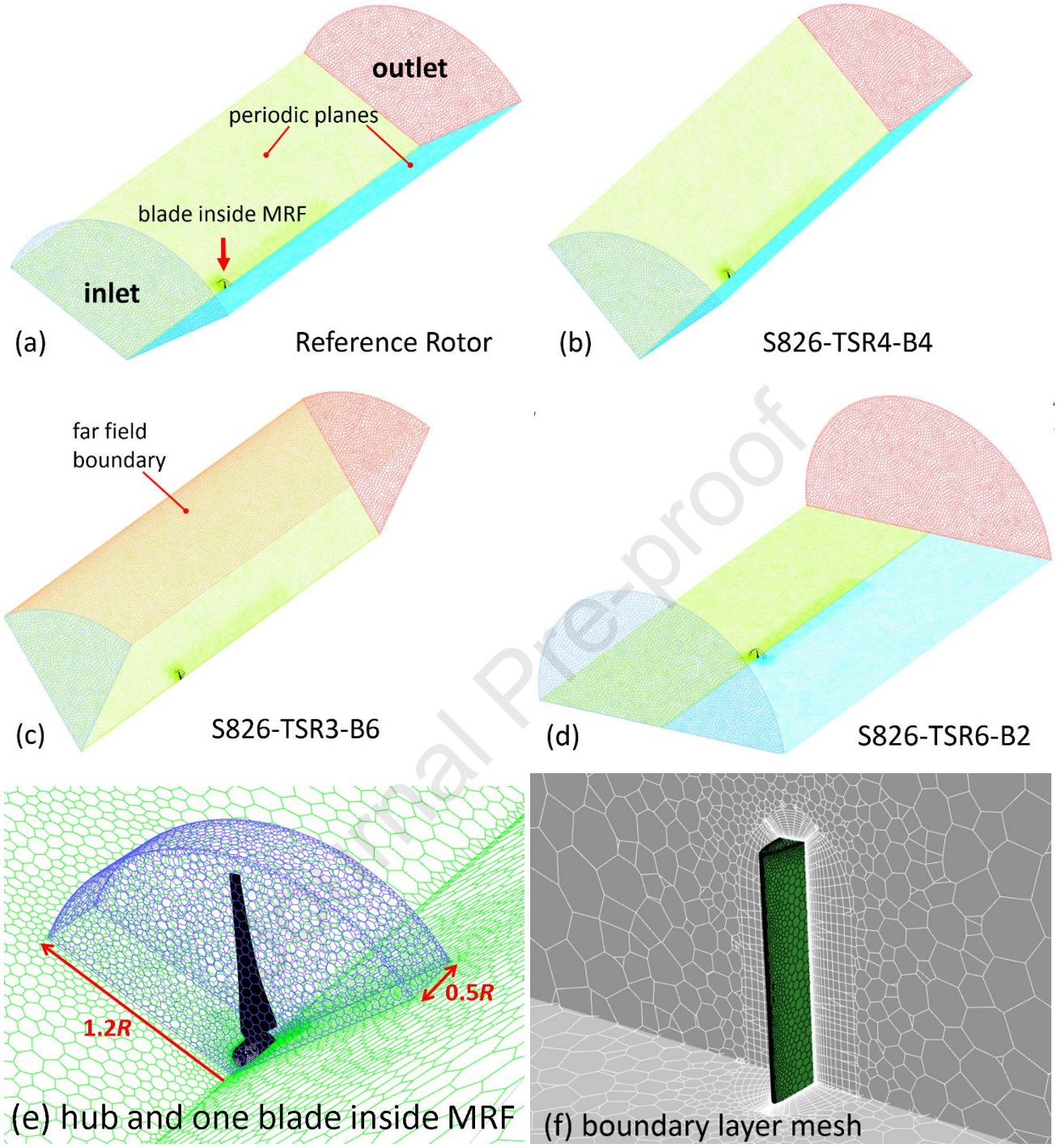

Fig. 7. Computational domains, boundaries and mesh structure.

To assess the impact of turbulence models, the performance of the Reference Rotor was predicted using different turbulence models [72,73]. For this purpose, the Spalart-Allmaras model and two-equation models standard k-ε, RNG k-ε, and SST k-ω were employed. The Spalart-Allmaras model, which is a one-equation model, includes a modeled transport equation for the kinematic turbulent viscosity [74]. Due to its success in capturing flow separation in boundary layer flows caused by adverse pressure gradients, the Spalart-Allmaras

model is preferred in turbomachinery analyses [75]. To better predict the influence of rotation on turbulence, a strain/vorticity-based approach was employed in the calculation of turbulence production [71].

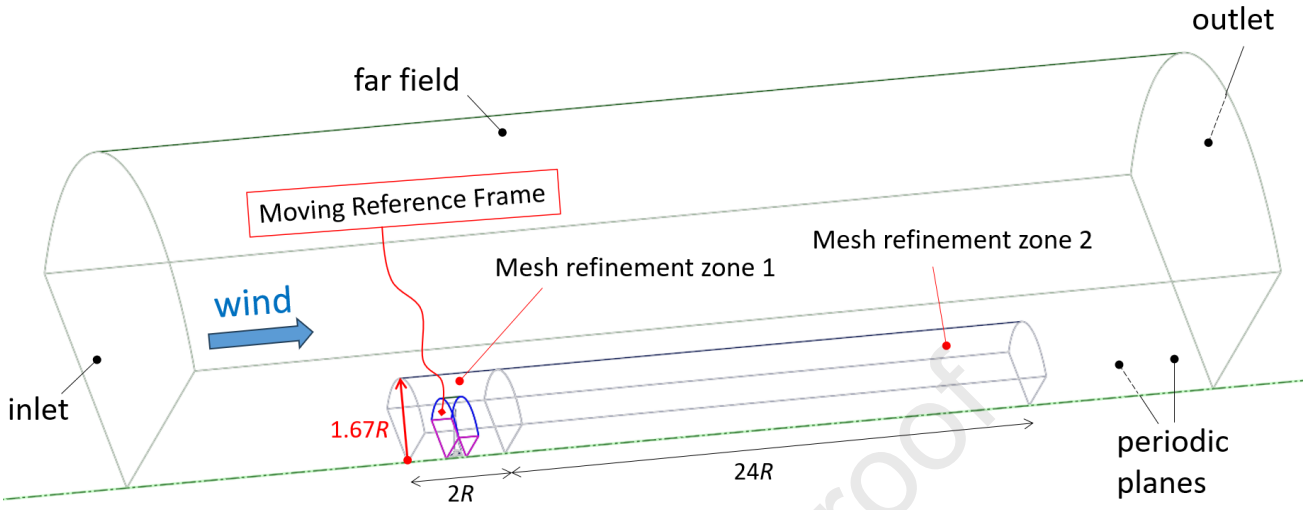

Fig. 8. The sizes of the mesh refinement zones (not to scale).

Table 4. The mesh particulars pertaining to the sensitivity study.

	Mesh count	1st layer thickness (mm)	y^+_{avg}	y^+_{max}
Mesh A	1,792,509	0.5	≈ 22	< 75
Mesh B	2,333,136	0.1	≈ 4.5	< 20
Mesh C	3,851,657	0.02	≈ 1	< 5
Mesh D	7,171,166	0.004	≈ 0.2	< 1

The standard k-ε model was also preferred in wind turbine analyses in the literature [73,76]. The RNG k-ε model [77,78] offers advantages over the standard k-ε model for a wider range of flows due to its ability to account for the effects of swirl on turbulence by modifying the turbulent viscosity. For standard and RNG k-ε models, the Menter-Lechner Enhanced Wall Treatment (EWT) model was used for near-wall modeling due to its preference over the two-layer EWT model for non-equilibrium flows with pressure gradients [71].

The SST k-ω model is less sensitive to free stream conditions and accounts for turbulence shear stress transport [79,80]. The SST k-ω model accurately predicted velocity profiles in separated flows caused by adverse pressure gradients, which matched well with experimental data [79]. The SST k-ω model has been widely used for aerodynamic analyses of wind turbines over the past few decades [70,73,81] and power performance prediction of SWTs in the range of 1 m diameter [29,82,83]. The SST k-ω model achieves a good balance of computational accuracy and computing time [84].

The CFD simulations used a similar mesh structure as employed by Yilmaz [11]. A boundary layer mesh was generated over the blade surfaces (Fig. 7f). The face mesh was in a polygon shape, while the computational domain consisted of polyhedral mesh elements, excluding prismatic boundary layer meshes [85]. To ensure proper control over the mesh sizes, two mesh refinement zones were established (Fig. 8). A sensitivity study on mesh density was conducted using the Reference Rotor, and the relevant mesh information is summarized in Table 4.

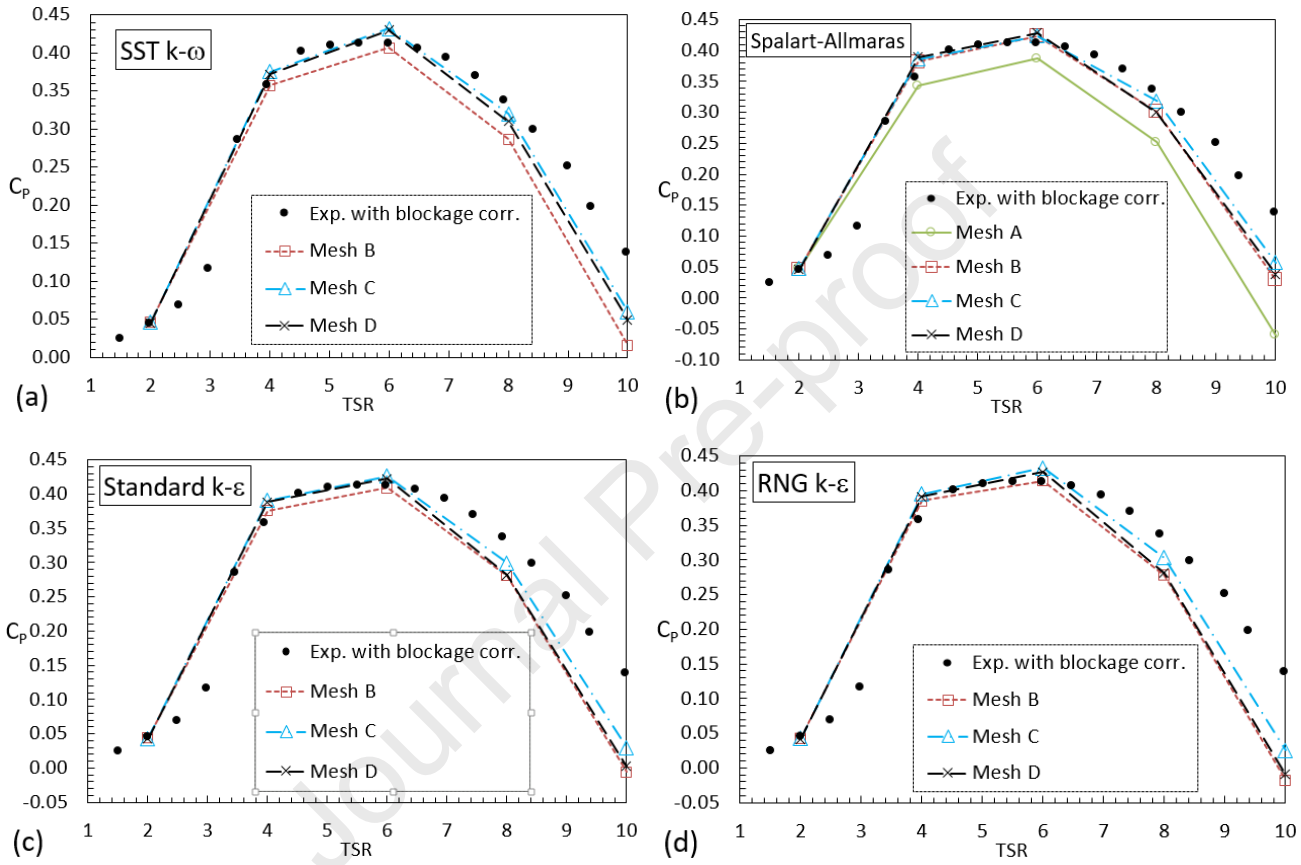

Fig. 9. The results of the mesh density sensitivity study performed for λ = 2, 4, 6, 8, and 10.

The power coefficient is determined by,

$$C_P = \frac{BQ_{blade}\Omega}{0.5\rho\pi R^2 U^3} \tag{21}$$

Here, Q_{blade} represents the torque acting on the blade. The air density (1.225 kg/m³) and viscosity (1.7894 × 10^{-5}) were considered under standard atmospheric conditions. When considering the entire λ range, Mesh C exhibited the best agreement with the experimental data for the four turbulence models (Fig. 9). The larger deviations of the densest mesh (Mesh D) relative to Mesh C may be attributable to its more stretched computational meshes over the blade surface.

The optimal mesh (Mesh C), with details summarized in Table 5, was employed for the comparison of CFD-BEM predictions in Section 3.3. The mesh counts for the computational domains of the Reference Rotor, 4-, 6-, and 2-bladed rotors were 3,851,657; 3,535,951; 3,476,490; and 3,926,529, respectively. The average y^+ over the blade was around 1, with y^+_{max} less than 6.

Table 5. The meshing parameters of the optimum mesh (Mesh C).

Blade surface mesh	Boundary layer	Volume mesh
min. face size : 0.2 mm	1st layer thickness : 0.02 mm	MRF : 25 mm (max. size)
max. face size : 1.6 mm	growth rate : 1.25	mesh refinement zones 1 & 2 : 50 & 100 mm (max. sizes)
growth rate : 1.2	number of layers : 20	whole computational domain : 200 mm (max. size)
		growth rate : 1.2

Figure 10 displays the results of the CFD simulations conducted on the Reference Rotor using Mesh C. The SST k-ω model produced results that were closest to the experimental data at both low and high λ ranges. While the C_P values predicted by the rest of the models were almost overlapping, the RNG k-ε model provided the second most accurate prediction. The mean absolute relative error (MARE, equation 22) values for the SST k-ω, RNG k-ε, standard k-ε, and Spalart-Allmaras models are 11.5%, 17.6%, 20.1%, and 20.6%, respectively, across the entire TSR range. The largest error, however, occurred at the highest λ = 10, where the rotor is less likely to operate throughout its lifetime [52]. Excluding this specific point, the MARE values would be 6.5%, 10.5%, 13.7%, and 14.1% for the SST k-ω, RNG k-ε, standard k-ε, and Spalart-Allmaras models, respectively. The SST k-ω model was deemed suitable for performance predictions of the optimum best C_P rotors in Section 3.3.

$$MARE = \frac{\sum_{i=1}^{M} \left| \left(C^i_{P,CFD} / C^i_{P,\exp} - 1 \right) \right|}{M} \tag{22}$$

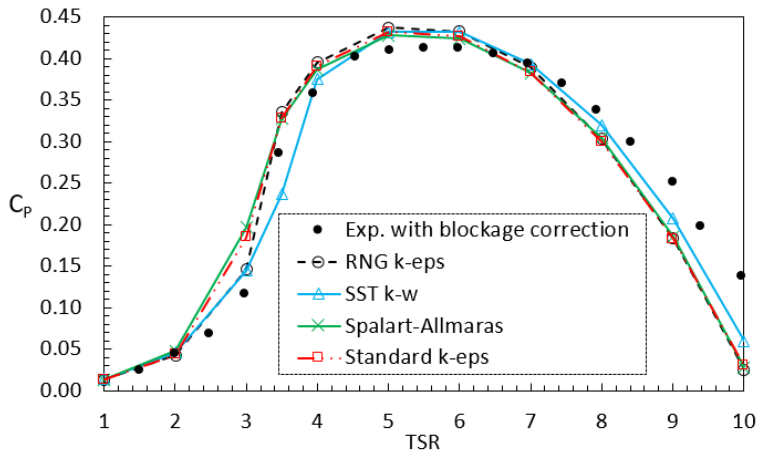

Fig. 10. Comparison of the predictions of turbulence models with experimental results of Ref. [58].

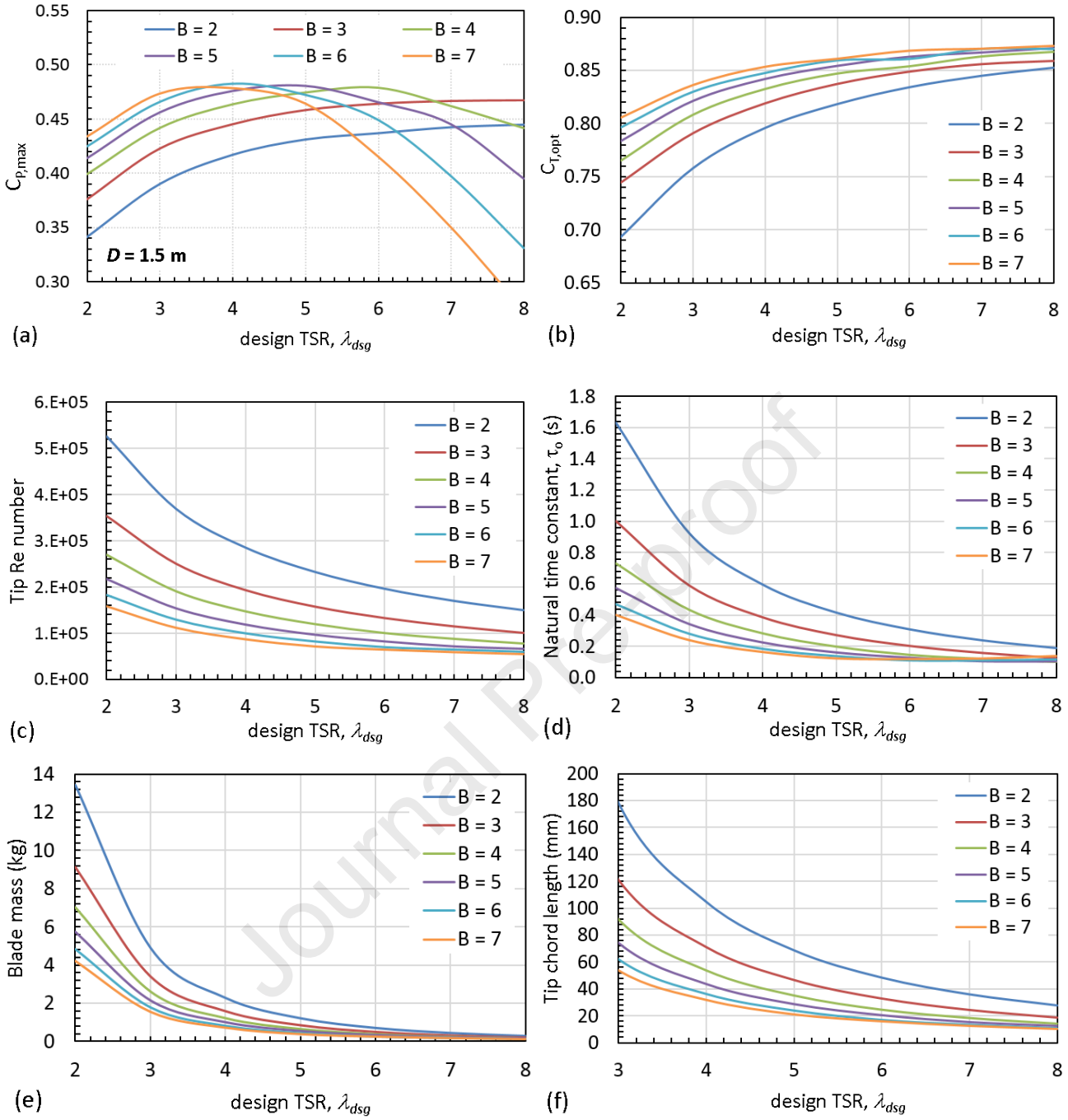

Fig. 11. Effect of B and λ_{dsg} on best C_P rotors' (a) $C_{P,max}$, (b) $C_{T,opt}$, (c) Re_{tip}, (d) τ_o, (e) blade mass, and (f) c_{tip}.

3 Results

3.1 1.5 m diameter best C_P rotors

3.1.1 Effects of design tip speed ratio and blade number on rotor design and performance

The design space for B was scanned from 2 to 7, and for λ_{dsg} from 2 to 8. In general, the highest $C_{P,max}$ is achieved at lower λ_{dsg} as B increases (Fig. 11a). $C_{P,max}$ of two- and three-bladed rotors rises with λ_{dsg} constantly in the investigated range, whereas $C_{P,max}$ of multi-bladed rotors (B = 4 to 7) declines after a specific λ_{dsg}. As λ_{dsg}

increases, the chord length decreases (Fig. 11f), resulting in a decrease in Re number (Fig. 11c). Consequently, multi-bladed rotors with relatively low Re numbers experience a decrease in $C_{P,max}$. It is worth noting that the efficiency of airfoil S826 decreases dramatically below Re = 10^5. At a fixed λ_{dsg}, the blade Re number also decreases with increasing B. The decrease in $C_{p,max}$ of multi-blade rotors almost coincides with the threshold Re number of 10^5. The highest $C_{P,max}$ values attained by two- and three-bladed rotors are noticeably lower, although their Re numbers never drop below 10^5. The most efficient rotors (with highest $C_{P,max}$) for varied B are listed in Table 6 and illustrated in Fig. 12. The six-bladed rotor achieved the greatest $C_{P,max}$ (0.483) with λ_{dsg} = 4, while the two-bladed rotor attained a 7.9% lower $C_{P,max}$ (0.445).

Table 6. Particulars of the most efficient rotors of 1.5 m diameter for varied B.

Rotors	Re	σ	RPM	τ_o	Blade inertia	Blade mass	$C_{T,opt}$	$C_{P,max}$	ΔC_P	$C_Q(\lambda=0)$
				s	kg.m^2	kg				
S826-TSR2-B12	94419	37.6%	255	0.23	0.4732	2.556	0.830	0.454	-6.0%	0.0876
S826-TSR3-B8	97896	22.2%	382	0.21	0.2003	1.376	0.841	0.477	-1.2%	0.0358
S826-TSR4-B6	99259	14.6%	509	0.19	0.1007	0.831	0.848	**0.483**	**Ref.**	0.0175
S826-TSR5-B5	96293	10.4%	637	0.16	0.0553	0.524	0.854	0.481	-0.4%	0.0096
S826-TSR6-B4	99950	7.7%	764	0.15	0.0351	0.371	0.854	0.479	-0.8%	0.0056
S826-TSR7-B3	114548	5.9%	891	0.16	0.0265	0.306	0.856	0.467	-3.3%	0.0034
S826-TSR8-B2	149231	4.7%	1019	0.19	0.0237	0.292	0.853	0.445	-7.9%	0.0021

Figure 11b shows that optimum C_T ($C_{T,opt}$) of the best C_P rotors rises with both B and λ_{dsg}. $C_{T,opt}$ of the most efficient rotors in Table 6 ranges between 0.830 and 0.856, with a maximum deviation of 3%. The rise in $C_{T,opt}$ of multi-bladed rotors at high λ_{dsg}, despite the decrease in $C_{P,max}$, is due to the increased contribution of drag force to thrust at lower Re. To recall, at the Betz limit (C_P = 0.593), an ideal turbine without energy loss has $C_{T,opt}$ of 8/9 [86].

The natural time constant (τ_o) serves as a useful metric to assess how quickly variable-speed turbines react to wind speed change [13,19]. τ_o is determined by the rotor inertia, rated angular speed, and rated aerodynamic torque.

$$\tau_o = \frac{\Omega_r}{3}\frac{J}{Q_r} \tag{23}$$

τ_o ranges from 1 s for small turbines to 10 s for MW scale turbines [19]. Figure 11d shows that as λ_{dsg} and B increase, τ_o decreases along with a reduction in blade mass (Fig. 11e). This implies that replacing the rotor with a multi-bladed one results in a more reactive turbine for the same λ_{dsg}, i.e. an existing generator. Blade mass and τ_o increase dramatically below λ_{dsg} = 3. Despite the significant difference in blade mass between the slowest rotor S826-TSR2-B12 (2.556 kg) and the fastest rotor S826-TSR8-B2 (0.292 kg), τ_o values of the most

efficient rotors fall within a narrow range (Table 6). Starting torque coefficient, on the other hand, increases from 0.0021 to 0.0876 as λ_{dsg} decreases.

Figure 13 depicts the C_P of the most efficient rotors as a function of TSR. High TSR rotors have a wider optimum TSR range because their blade attack angles are less sensitive to changes in TSR, resulting in slower deviations from the design AoA, particularly at low λ [11]. Considering the literature discussion in the introduction, evaluating the performance characteristics in relation to wind speed variations would provide valuable insights.

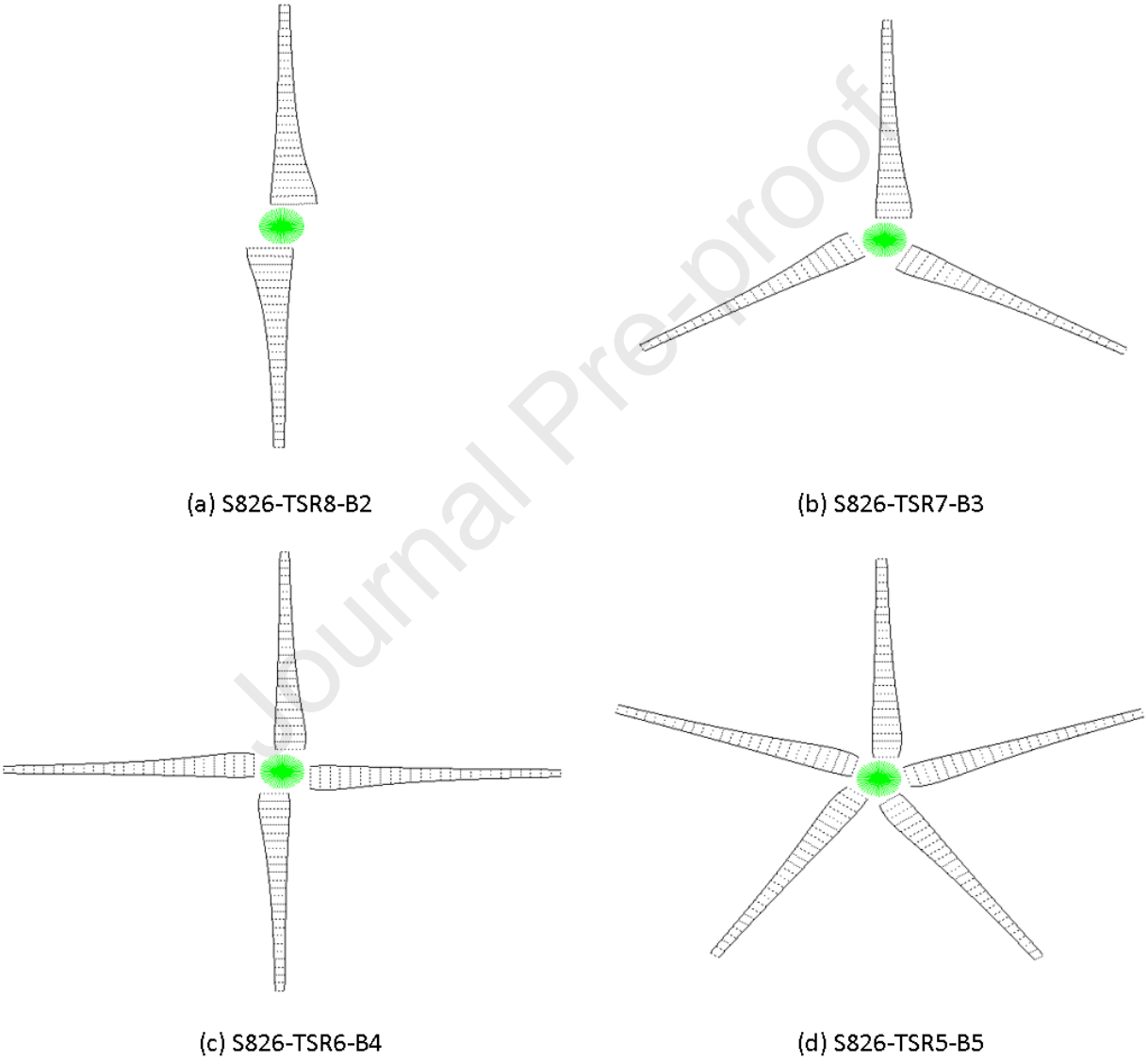

Fig. 12. (Continued) The most efficient rotors of 1.5 m diameter for varied *B*.

The BEM algorithm was executed at wind speeds ranging from 4 to 20 m/s, maintaining a constant rotor speed corresponding to the optimum RPM for U_{dsg} = 10 m/s. At low wind speeds, low-speed rotors exhibit substantially higher C_P (Fig. 14a). One key reason for this is that low-speed rotors' tip speed ratio deviates from

λ_{dsg} significantly less (Fig. 14b). A simple examination will show that this is the case. By noting that $\lambda = \Omega R/U$, the derivative of the tip speed ratio with respect to varying wind speed can be determined for constant Ω.

$$\left.\frac{\partial \lambda}{\partial U}\right|_{\Omega=const} = -\frac{\Omega R}{U^2} \tag{24}$$

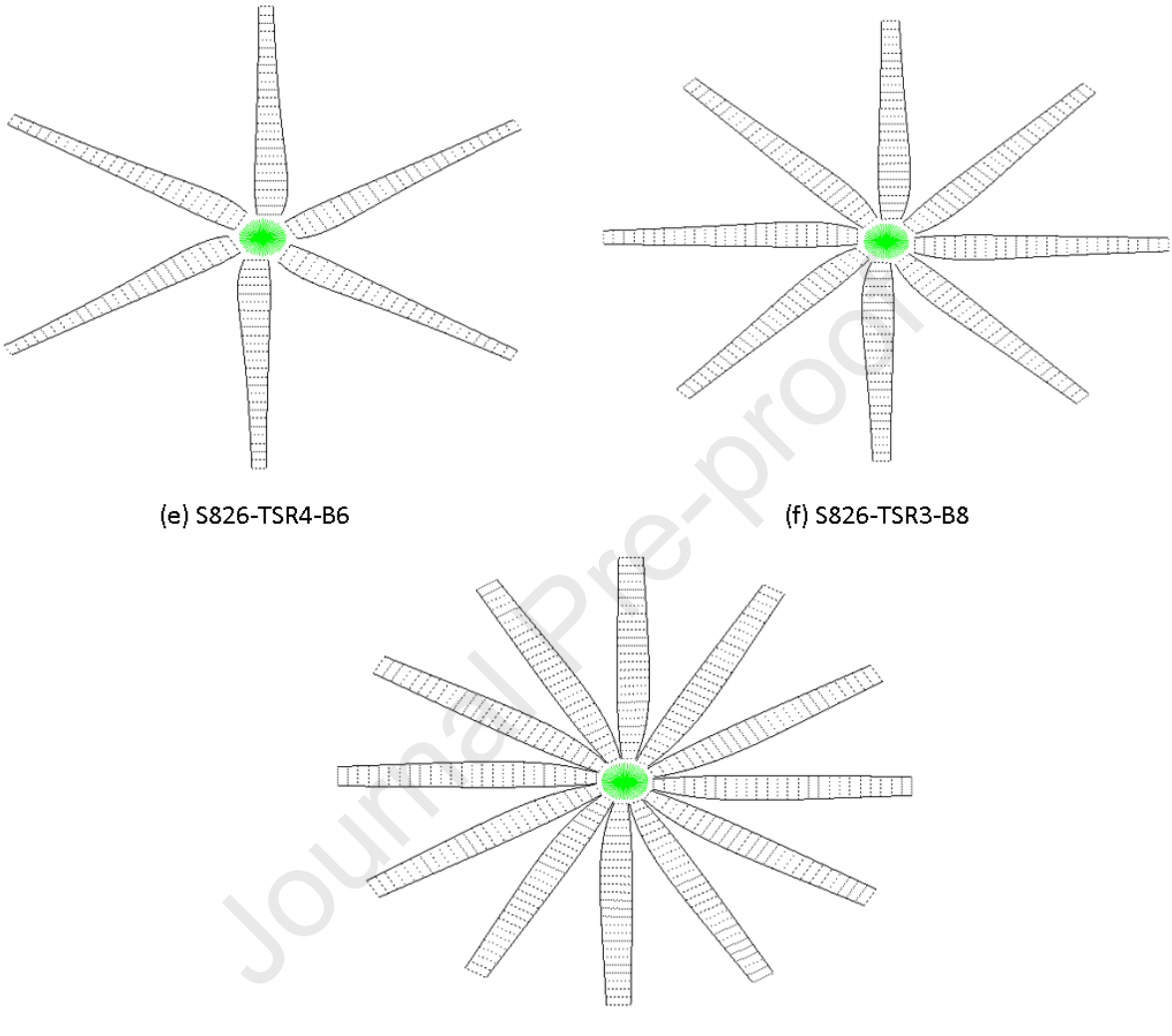

(e) S826-TSR4-B6 (f) S826-TSR3-B8

(g) S826-TSR2-B12

Fig. 12. The most efficient rotors of 1.5 m diameter for varied *B*.

As can be evident, the instant operational TSR of high-speed rotors (high λ_{dsg}, high Ω) must vary more in response to wind speed change. In line with this finding, Yang et al. [22] showed, through dynamic rotor analysis of a variable-speed MW scale turbine, that the instantaneous TSR of low TSR rotor varied within a narrow range compared to high TSR rotor. Figures 14c and 14d show the axial induction factor and AoA at *r/R* = 0.8, representing the location with the greatest contribution to rotor power. High-speed rotors with λ_{dsg} = 5 to 8 exhibit considerably higher *a* at low wind speeds (high λ), indicating less wind flow and thereby insufficient energy capture, another indicator of lower efficiency (Fig. 14d). The axial induction factor of the low-speed rotor S826-TSR3-B8 closely approaches the optimum of an ideal rotor (a_{opt} = 1/3) [87] across a wide wind speed

range. On the other hand, low-speed rotors show greater variation in blade AoA across all wind speeds, with a notable increase in high wind speeds (low λ) (Fig. 14c). This explains their lower C_P at high wind speeds, although deviating less from λ_{dsg}.

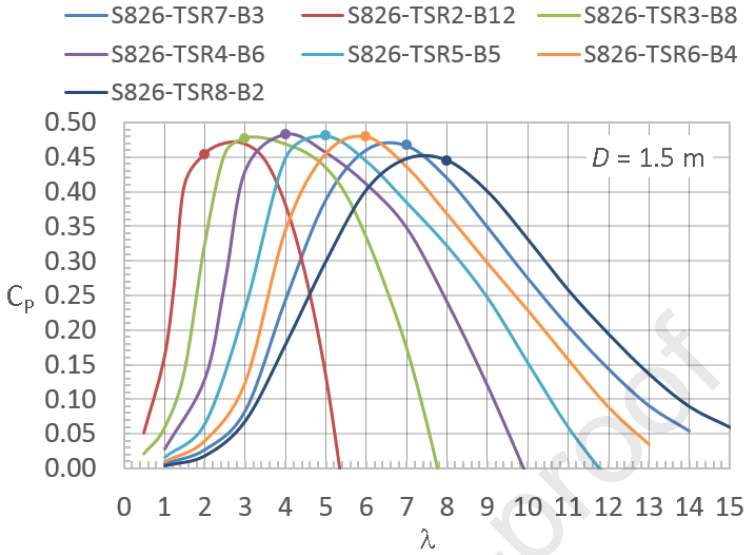

Fig. 13. C_P versus λ of the most efficient rotors. (U = 10 m/s)

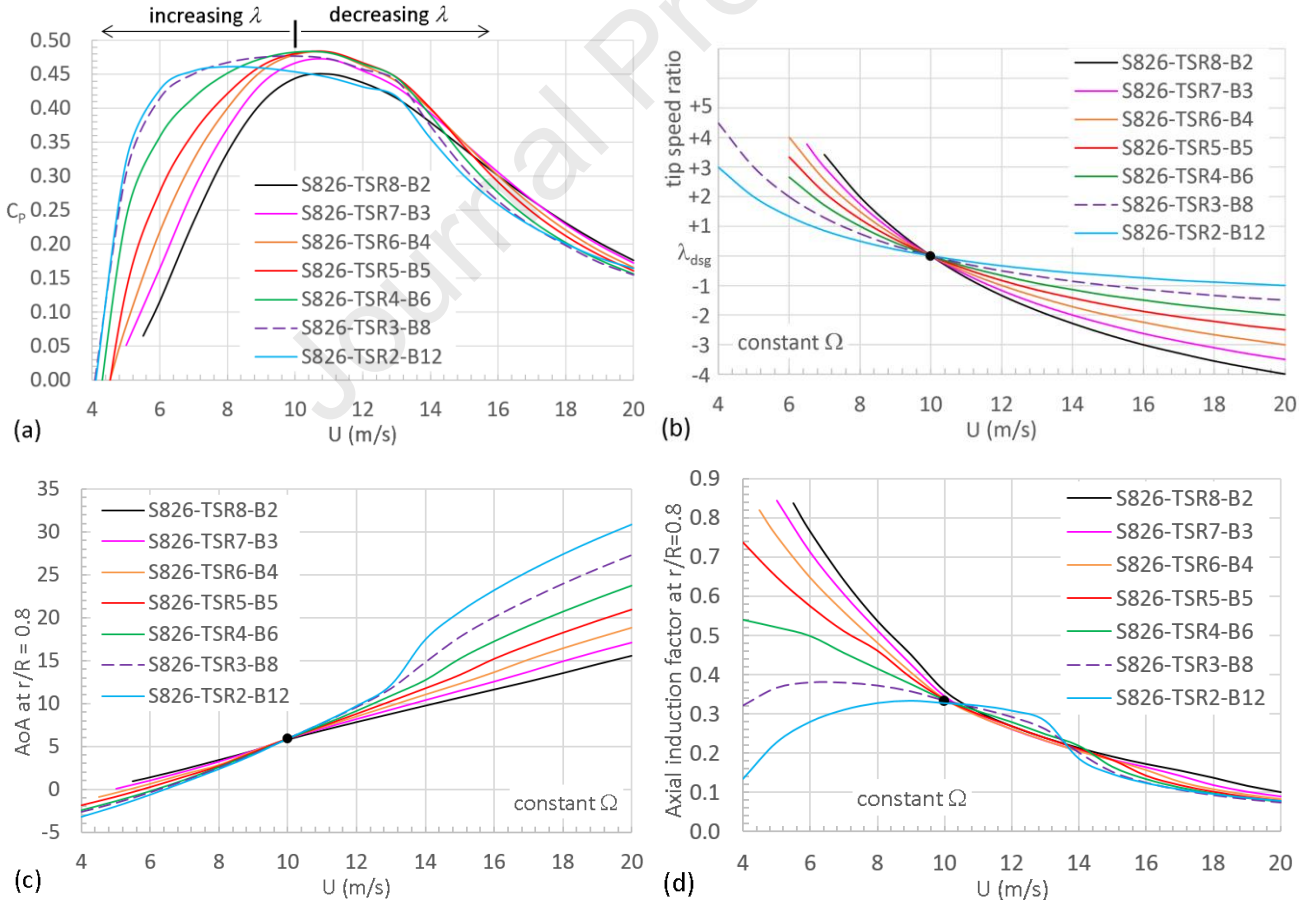

Fig. 14. Performance parameters of the most efficient rotors for varying wind speed at constant RPM, (a) C_P, (b) tip speed ratio, (c) AoA at r/R = 0.8 (d) a at r/R = 0.8. $RPM = 30U_{dsg}\lambda_{dsg}/\pi R$. The curves represent the parameter values in response to a deviation in wind speed from U_{dsg} = 10 m/s.

The Gaussian distribution well represents the probability distribution of the short term (1-min or 10-min) wind speeds around the mean [12].

$$f\left(U\right)=\frac{1}{\sigma\sqrt{2\pi}}e^{-\frac{1}{2}\left(\frac{U-U_{mean}}{\sigma}\right)^2} \tag{25}$$

Here σ is the standard deviation. TI ($=\sigma/U_{mean}$) may range from 0.1 to 0.6 in an urban setting [25,30]. To quantify the off-design performance of the rotors, an index designated as OPI for short was introduced and calculated for varying TI (Fig. 15).

$$OPI=\frac{\int_{U_{lower}}^{U_{upper}}0.5\rho C_P\pi R^2\,fU^3dU}{\int_{U_{lower}}^{U_{upper}}0.5\rho\pi R^2\,fU^3dU}=\frac{\int_{U_{lower}}^{U_{upper}}C_P\,fU^3dU}{\int_{U_{lower}}^{U_{upper}}fU^3dU} \tag{26}$$

OPI represents the ratio of rotor power to wind power within the wind speed range of U_{lower} (4 m/s) to U_{upper} (20 m/s). Rotors with λ_{dsg} = 4, 5, 6 maintained the highest OPI values across all TI levels. As TI increases, the OPI values of the 3-blade S826-TSR7-B3 become more comparable to these rotors. The examination suggests that proper choice of λ_{dsg} is essential for maximizing the energy capture from the turbulent wind in variable-speed turbines. This should also apply to constant-speed turbines.

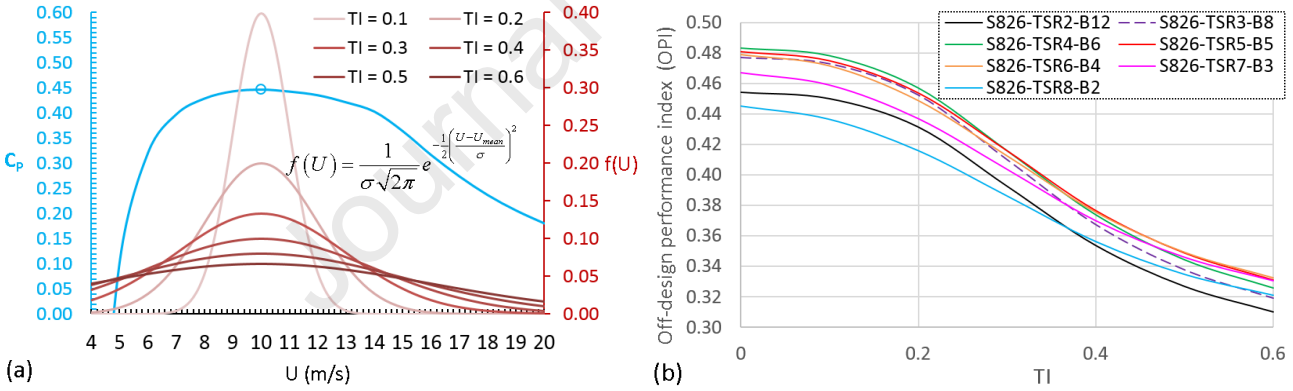

Fig. 15. (a) Wind speed frequency for varying TI. (b) OPI values of the most efficient rotors.

3.1.2 Low induction rotor

As illustrated in Fig. 16, the blades simply rotate a few degrees towards the incoming wind, reducing local AoA and wind resistance, leading to a decrease in the axial induction factor. In this way, a small decrease in $C_{P,max}$ and a large decrease in $C_{T,opt}$ can be achieved. As indicated by one-dimensional momentum analysis, changes in a around the best efficiency point of the Betz rotor cause a minor drop in C_P while yielding significant variation in C_T [88].

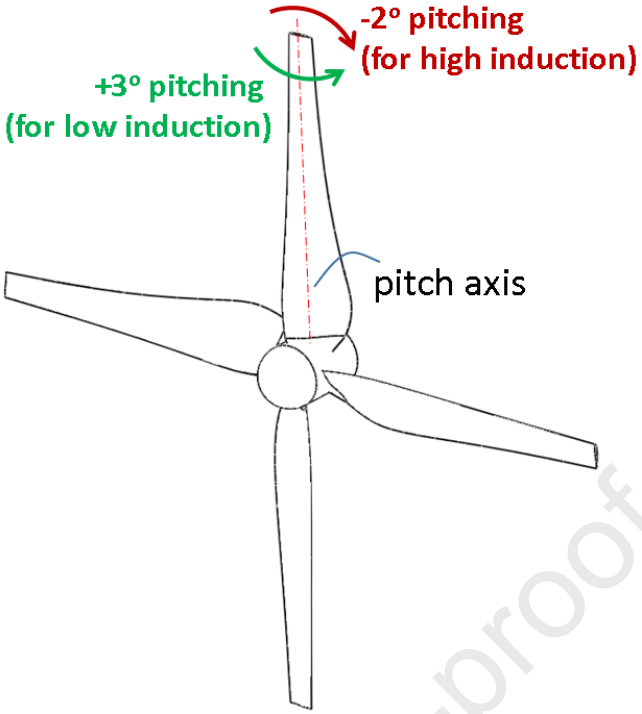

Fig. 16. Illustration of low and high induction rotors.

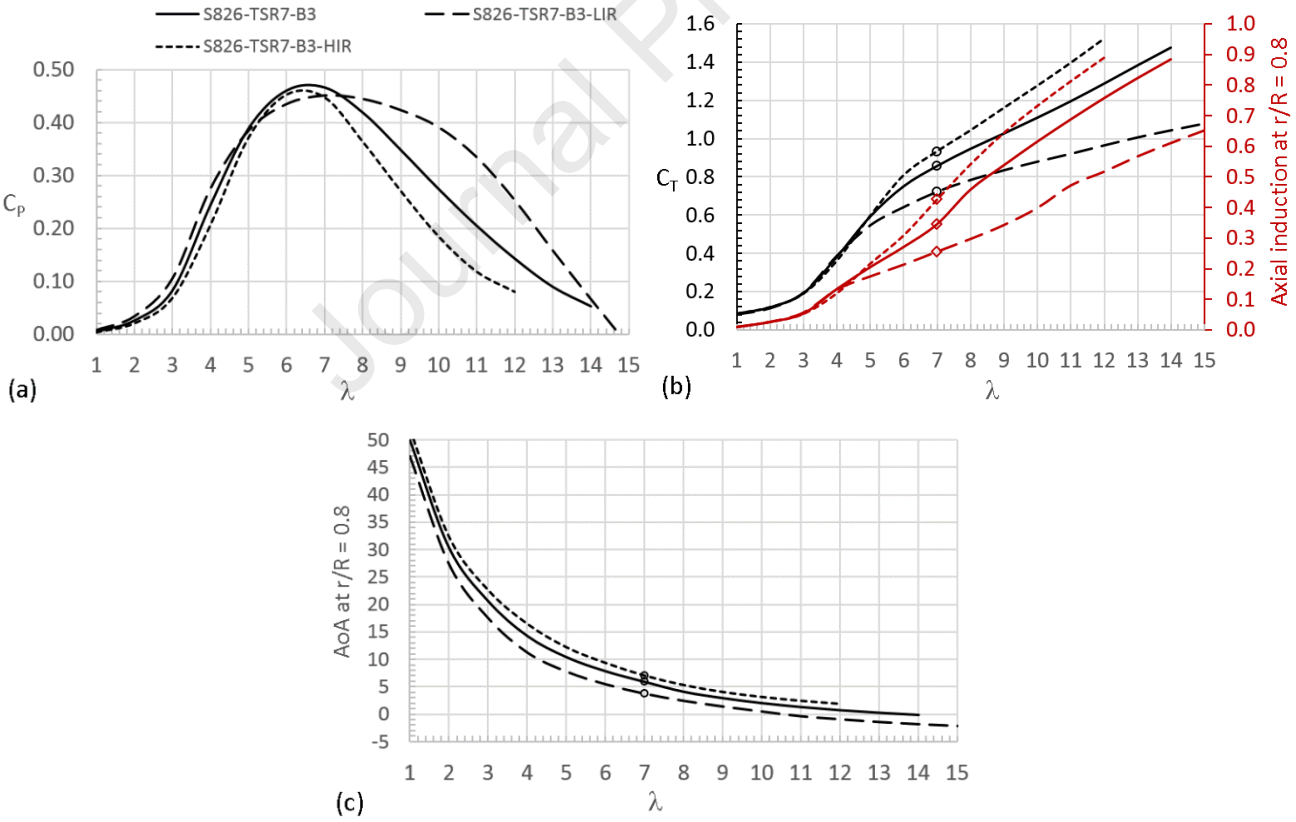

Fig. 17. Performance parameters of low and high induction rotors of S826-TSR7-B3, (a) C_P, (b) C_T, and a at r/R = 0.8. (c) AoA at r/R = 0.8.

Journal Pre-proof

Due to these noteworthy impacts, low induction option of the best C_P rotors was investigated. Beside, high induction rotor (HIR) was only studied for S826-TSR7-B3. A pitch angle change of +3° was adopted for LIRs, as larger increments resulted in a significant decrease in $C_{P,max}$. The pitch angle change of HIR was set to -2°. Although $C_{P,max}$ of the low induction rotor S826-TSR7-B3 being 3.5% lower than that of the 0° pitched original rotor, optimum TSR range extended for both low and high λ (Fig. 17a). As well, $C_{T,opt}$ of the LIR decreased by 15.7% from 0.856 to 0.722 (Fig. 17b). In response to the C_T drop in the mid- and high-tip speeds, a of the LIR reduced considerably within this range. Throughout the entire TSR range, the LIR's blade attack angle is smaller than that of the original rotor (Fig. 17c). This led to a decrease in post-stall angles at low λ, which increased blade efficiency and, consequently, C_P. Since all operational parameters changed against HIR, i.e. C_T, a, and local AoA increased at all tip speeds, C_P decreased over the entire TSR range.

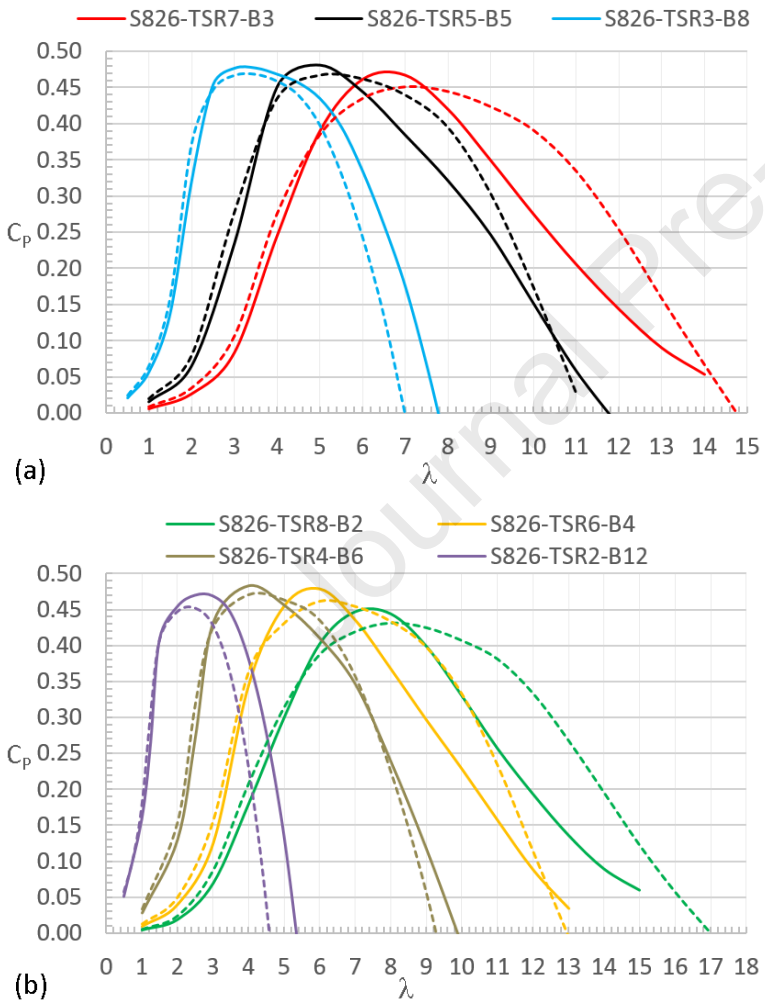

Fig. 18. C_P versus λ of the most efficient rotors (continuous line, —) and their low induction counterparts (dashed line, – –).

Figure 18 displays λ–C_P curves of the most efficient rotors and their low induction counterparts. The higher the λ_{dsg}, the broader the optimum TSR range offered by the low induction feature (refer to S826-TSR7-B3 and S826-TSR8-B2). $C_{P,max}$ of the high-speed rotors, however, suffered the most from the LIR option. Low-speed

rotors S826-TSR2-B12 and S826-TSR3-B8 showed reduced C_P at high tip speeds with low induction. This occurred because their axial induction factors, which already close to a_{opt} (1/3), fell below a_{opt} at high λ. For instance, a of S826-TSR3-B8 decreased from 0.40 at λ = 7 to 0.18 with low induction. Higher wind permeability led to suboptimal wind energy capture, resulting in lower C_P.

Figure 19 gives U-C_P curves of the most efficient rotors and their low induction counterparts. With the exception of the slowest rotors S826-TSR2-B12 and S826-TSR3-B8, the high C_P wind speed ranges of the LIRs expanded at the expense of some loss in $C_{P,max}$ (Figures 19a-c). It should be noted that the slowest LIRs would require a higher cut-in speed for constant-speed operation. Most LIRs exhibit greater C_P than the 3-blade high-speed rotor S826-TSR7-B3 at high and particularly low wind speeds.

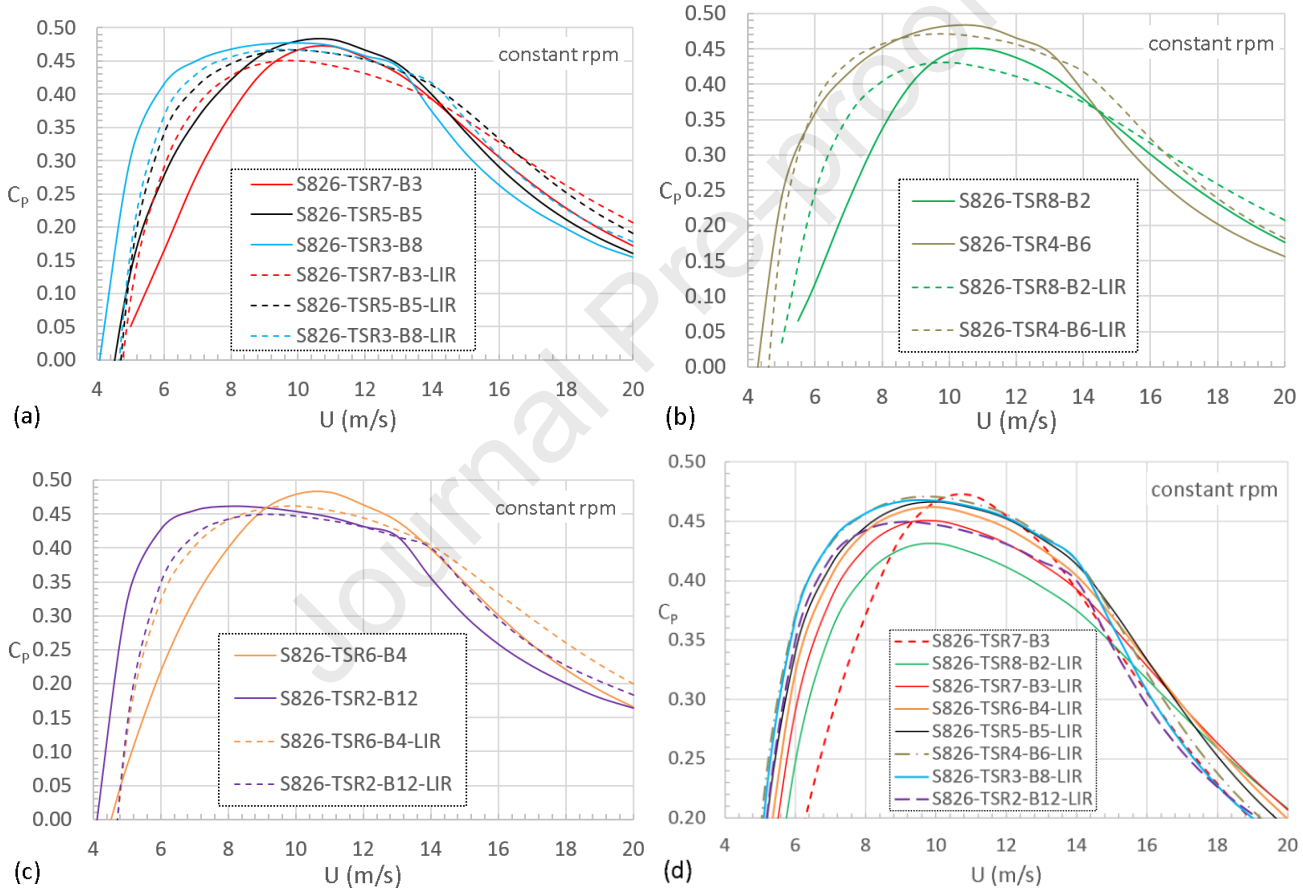

Fig. 19. U versus C_P curves of the most efficient rotors and their low induction counterparts at constant RPM. (d) LIRs are compared to S826-TSR7-B3.

In terms of the OPI values, S826-TSR4-B6-LIR and S826-TSR5-B5-LIR showed the best off-design performance (Fig. 20). With the exception of S826-TSR2-B12-LIR and S826-TSR8-B2-LIR, the LIRs exhibited better off-design performance than the 3-blade rotor S826-TSR7-B3. S826-TSR7-B3-LIR achieved a higher OPI value than S826-TSR7-B3 when TI exceeded 0.3, indicating that LIRs have the potential to capture more energy from turbulent winds above a threshold TI level. Consistent with this inference, Rocha et al. [42] observed in a field test

conducted at TI of 0.22 to 0.38 that increasing the blade pitch of a 3 m variable-speed turbine by +3° improved off-design aerodynamic efficiency.

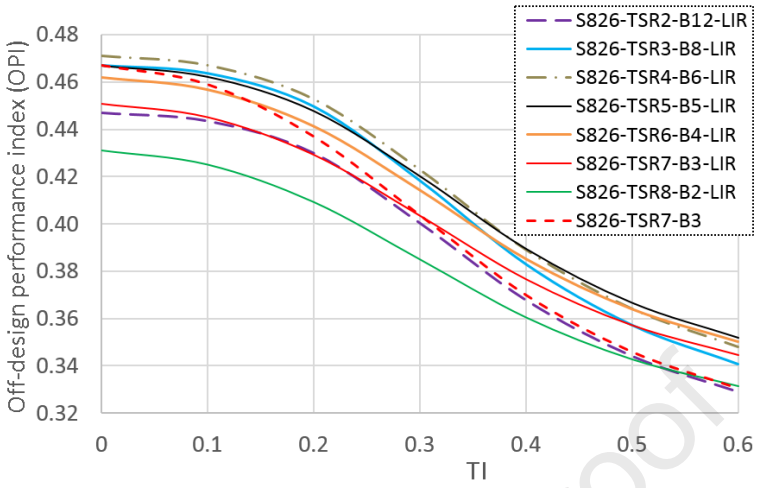

Fig. 20. The OPI values of LIRs and the 3-blade high-speed rotor S826-TSR7-B3.

3.1.3 Starting capability

For a relative comparison of rotors, the starting time (T_s) was defined as the time needed for rotors to reach λ = 1 at a steady wind speed. This study, like previous research [18,33], used a wind speed of 5 m/s, which represents the upper limit of the lowest wind power density category [12]. Considering the linear-like change in Ω during the idling period [17], a time step of Δt = 0.1 s was chosen for adequate resolution in reporting. Even during rapid acceleration, this time step consistently produced convergent results, indicating its conservative value. The starting wind speed (U_s) was estimated using a ramp function, gradually increasing the wind speed to 5 m/s linearly within 5 s. Since modern SWTs can be manufactured with zero generator cogging torque [15], starting times for Q_r = 0 Nm were also predicted.

Table 7. Starting times and wind speeds of the most efficient rotors and the LIRs.

Rotors	T_s (s)		U_s (m/s)	LIRs	T_s (s)		U_s (m/s)
	Q_r = 0	Q_r = 0.17 Nm			Q_r = 0	Q_r = 0.17 Nm	
S826-TSR8-B2	3.1	no start	n/a	S826-TSR8-B2-LIR	1.9	no start	n/a
S826-TSR7-B3	2.2	no start	n/a	S826-TSR7-B3-LIR	1.5	no start	n/a
S826-TSR6-B4	1.8	no start	n/a	S826-TSR6-B4-LIR	1.3	no start	n/a
S826-TSR5-B5	1.6	8.2	5	S826-TSR5-B5-LIR	1.2	3	4
S826-TSR4-B6	1.6	2.8	3.7	S826-TSR4-B6-LIR	1.3	2	3.2
S826-TSR3-B8	1.6	2	2.6	S826-TSR3-B8-LIR	1.3	1.6	2.5

As λ_{dsg} decreased, both T_s and U_s reduced (Table 7). Insufficient starting torque prevented high-speed rotors with λ_{dsg} = 6, 7, 8 from initiating rotation. The low-speed rotor S826-TSR3-B8 achieved lowest U_s at 2.6 m/s. The LIRs offered an essential operational choice, further lowering U_s and T_s with increment in blade pitch.

Overall, LIRs are well-suited for turbulent environments as they provide high efficiency across a wide range of wind speeds, while lowering the T_s and U_s. In low wind regions, S826-TSR3-B8-LIR and S826-TSR4-B6-LIR are reasonable options since they have better off-design performance with high $C_{P,max}$, as well as the lowest U_s and T_s. S826-TSR4-B6-LIR and S826-TSR5-B5-LIR are preferable in windy regions since they retain high C_P over the whole wind speed range and have the highest OPI values for all TI levels.

3.2 Effect of rotor diameter

Peak efficiency contour plots for the best C_P rotors were produced across the λ_{dsg}-B design space for diameters of 0.9, 1.5, 2, and 3 m (Fig. 21). The peak efficiency increases with diameter, and the design sub-space for high aerodynamic efficiency expands. Larger diameter rotors necessitate more blades for attaining the greatest $C_{P,max}$. The most efficient 0.9 m diameter rotor, S826-TSR4-B4, has $C_{P,max}$ = 0.456, 9% lower than the most efficient 3 m diameter rotor, S826-TSR4-B12 ($C_{P,max}$ = 0.504). Appendix A includes λ_{dsg}-$C_{P,max}$ curve families.

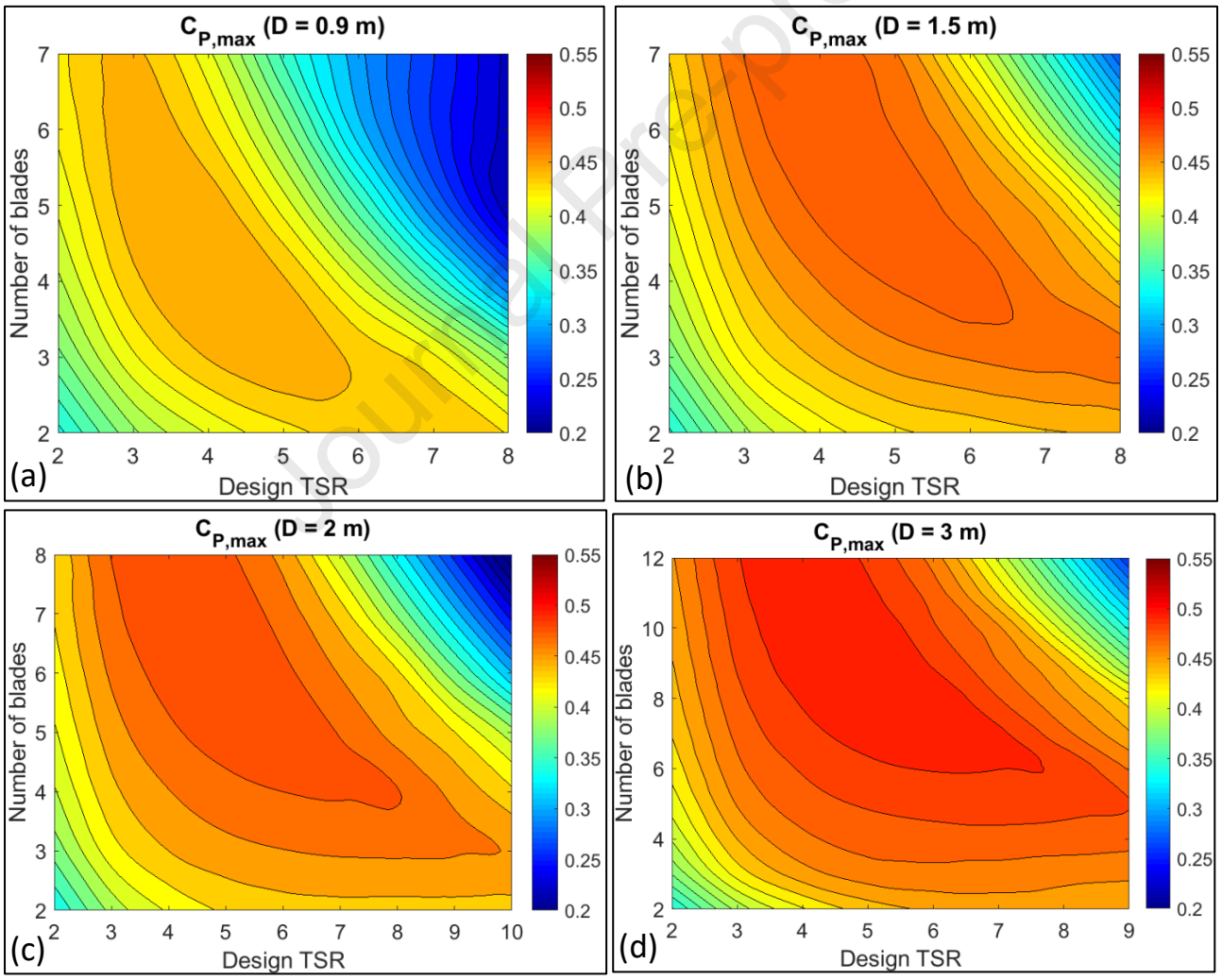

Fig. 21. $C_{P,max}$ of the best C_P rotors for (a) D = 0.9 m, (b) D = 1.5 m, (c) D = 2 m and, (d) D = 3 m.

3.3 0.9 m diameter best C_P rotors

The performances of the 0.9 m diameter best C_P rotors are compared to the Reference Rotor [58] from Section 2.1.2. Figure 22 depicts blade chord and pitch distributions of the rotors. The single parameter that affects the pitch distribution of the best C_P blade, regarding to equation (10), is λ_{dsg}. The pitch distributions between the Reference Rotor and S826-TSR6-B2 (having the same λ_{dsg}) show significant disparities throughout the blade span, although they overlap at the tip. The pitch angles are believed to be increased to improve the starting behavior of the Reference Rotor, resulting in a lower $C_{T,opt}$, and giving it a low induction feature (Fig. 23). The $C_{P,max}$ (0.456) of S826-TSR4-B4 is 7.3% greater than that of the Reference Rotor (0.425).

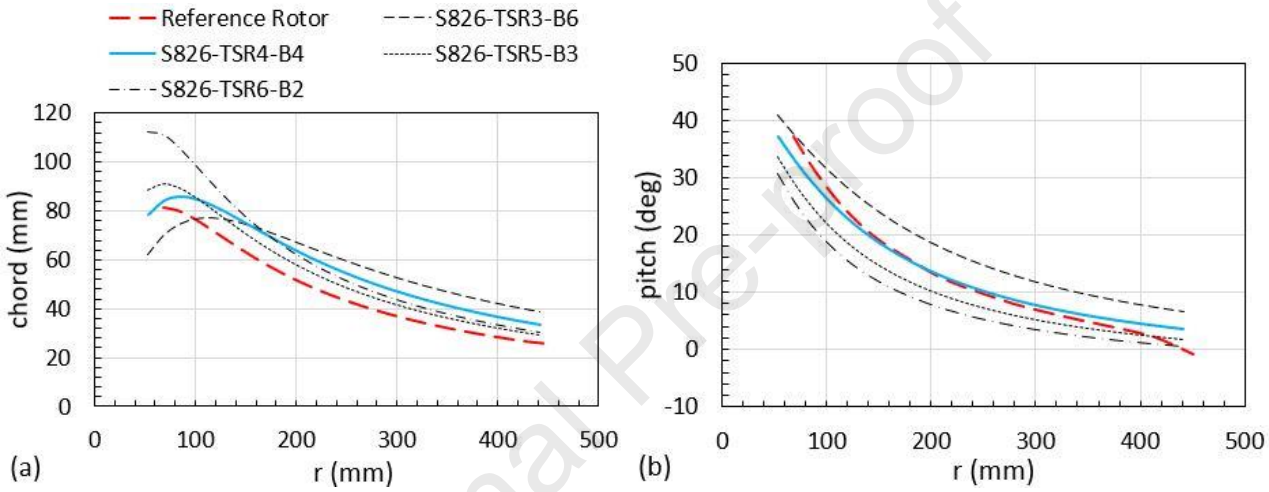

Fig. 22. (a) Chord, and (b) pitch distributions of the Reference Rotor and 0.9 m diameter best C_P rotors.

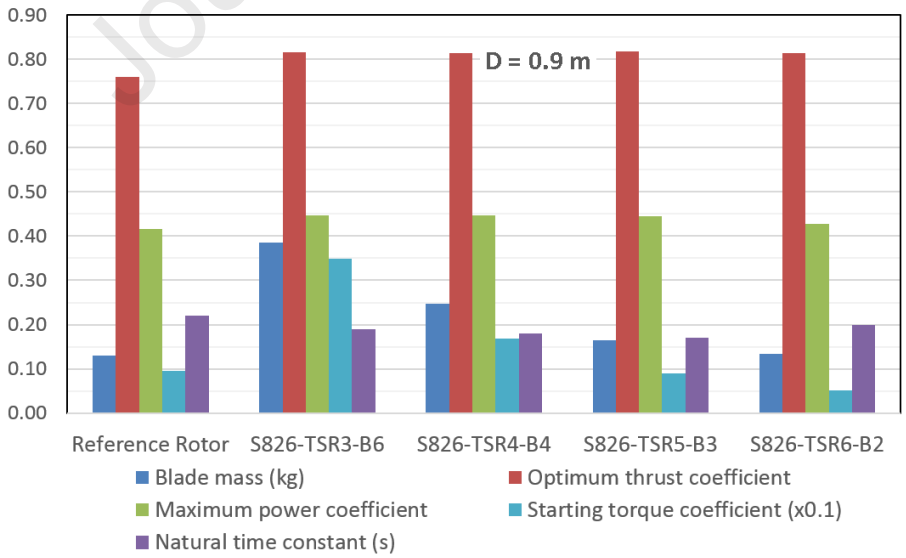

Fig. 23. Performance metrics and blade masses of the 0.9 m diameter best C_P rotors and the Reference Rotor.

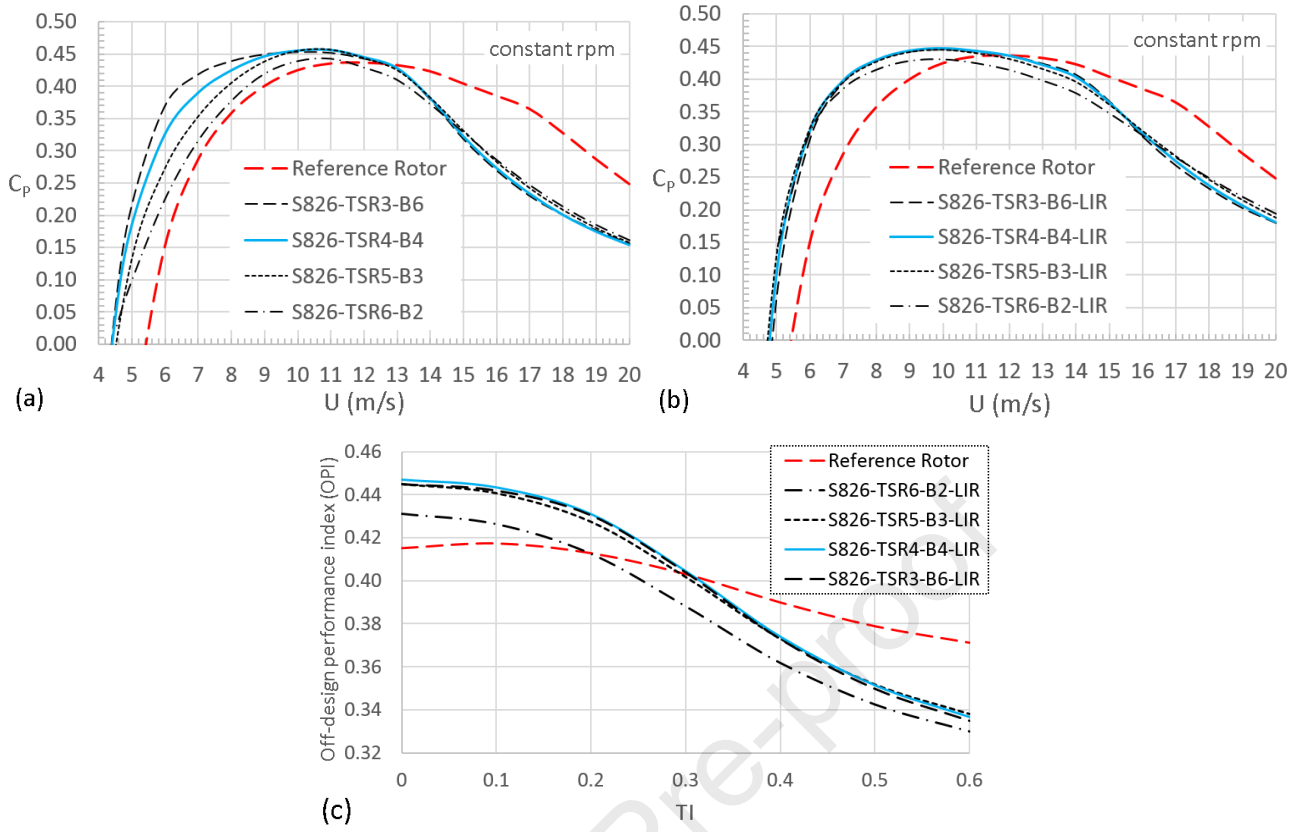

Fig. 24. *U* versus C_P curves of (a) the 0.9 m diameter best C_P rotors, and (b) the LIRs. c) LIRs' OPI values.

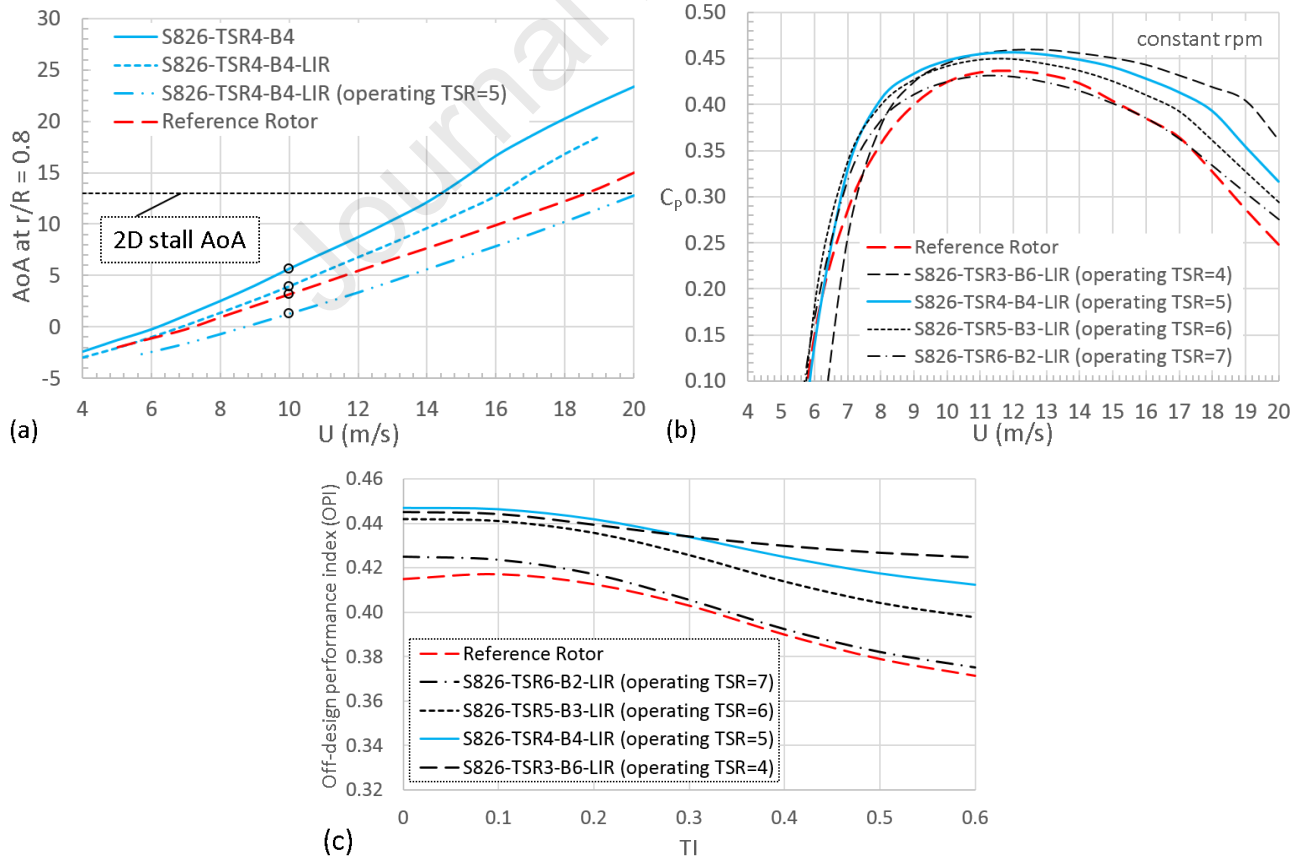

Fig. 25. (a) AoA at r/R = 0.8, and (b) *U* versus C_P curves of LIRs with $\lambda_{ope} = \lambda_{dsg} + 1$. (c) OPI values.

The best C_P rotors have lower C_P at high wind speeds but exhibit higher efficiency at low wind speeds compared to the Reference Rotor (Fig. 24a). The Reference Rotor blades stall later due to their higher speed and increased pitch angles (Fig. 25a). Although the LIRs improved C_P at high wind speeds, they still fell short of the Reference Rotor (Fig. 24b). The OPI values of LIRs substantially decreased above a TI level of 0.3 (Fig. 24c).

To improve C_P at high wind speeds, operating TSR (λ_{ope}) of the LIRs was shifted by +1. Blade AoA of low induction rotor with $\lambda_{ope} = \lambda_{dsg} + 1$ stays below that of the Reference Rotor and the stall AoA (Fig. 25a). Excluding S826-TSR6-B2-LIR, the LIRs offer much higher C_P at high wind speeds (Fig. 25b). In terms of OPI values, the performance degradation of LIRs in off-design conditions is significantly reduced (Fig. 25c).

In the case of zero generator cogging torque, the Reference Rotor exhibits the lowest T_s in both normal and low induction configurations (Table 8). In the case of non-zero cogging torque, Reference Rotor starts much later than the low-speed rotors, with T_s = 17.7 s, and the starting wind speed (U_s = 5 m/s) is rather high. The low induction option significantly improves the Reference Rotor's T_s, reducing it to 3.6 s. Pitching by 3°, on the other hand, would decrease $C_{P,max}$ by 9.6% for the Reference Rotor, which already has a low induction nature.

Table 8. Starting times and wind speeds of the 0.9 m diameter best C_P rotors and the LIRs. Comparison with the Reference Rotor.

Rotors	T_s (s)		U_s (m/s)	LIRs (+3° pitched)	T_s (s)		U_s (m/s)
	Q_r = 0	Q_r = 0.04 Nm			Q_r = 0	Q_r = 0.04 Nm	
Reference Rotor	1.4	17.7	5	Reference Rotor-LIR	1.1	3.6	4.3
S826-TSR6-B2	2.3	no start	n/a	S826-TSR6-B2-LIR	1.6	no start	n/a
S826-TSR5-B3	1.7	no start	n/a	S826-TSR5-B3-LIR	1.3	4.3	4.2
S826-TSR4-B4	1.6	3	3.7	S826-TSR4-B4-LIR	1.3	2.1	3.4
S826-TSR3-B6	1.4	1.8	2.7	S826-TSR3-B6-LIR	1.2	1.4	2.5

S826-TSR3-B6-LIR, with the lowest U_s (2.5 m/s) while maintaining the highest $C_{P,max}$, would be the preferable choice in low wind regions. To improve off-design performance, the rotor may benefit from optimizing the increment in operational TSR (Fig. 25b). In windy regions, S826-TSR4-B4-LIR with λ_{ope} = 5 would be the ideal choice because it maintains high C_P across almost the whole wind speed range and suggests high OPI values at all TI levels. Figure 26 displays the three-dimensional geometry of the 0.9 m diameter *optimum* best C_P rotors.

BEM performance predictions for the optimum best C_P rotors and their low induction counterparts showed satisfactory agreement with the CFD results (Figures 27a and 27b). Due to radial expansion and wake entrainment, the flow velocity increases in the outer part of the rotor [81,87]. The streamtube-based method BEM, which ignores radial interactions, overestimates a in the tip region, leading to an underprediction of $C_{P,max}$ [11]. Both the S826-TSR6-B2 and the Reference Rotor showed similar discrepancies between BEM and CFD predictions, although the deviations are larger (refer to Fig. 27c and 5). Yet, CFD simulations agreed that

the LIR improved off-design aerodynamic efficiency. CFD confirmed that multi-blade rotor with an increased operational TSR outperformed the 3-blade rotor over the entire wind speed range (Fig. 27d).

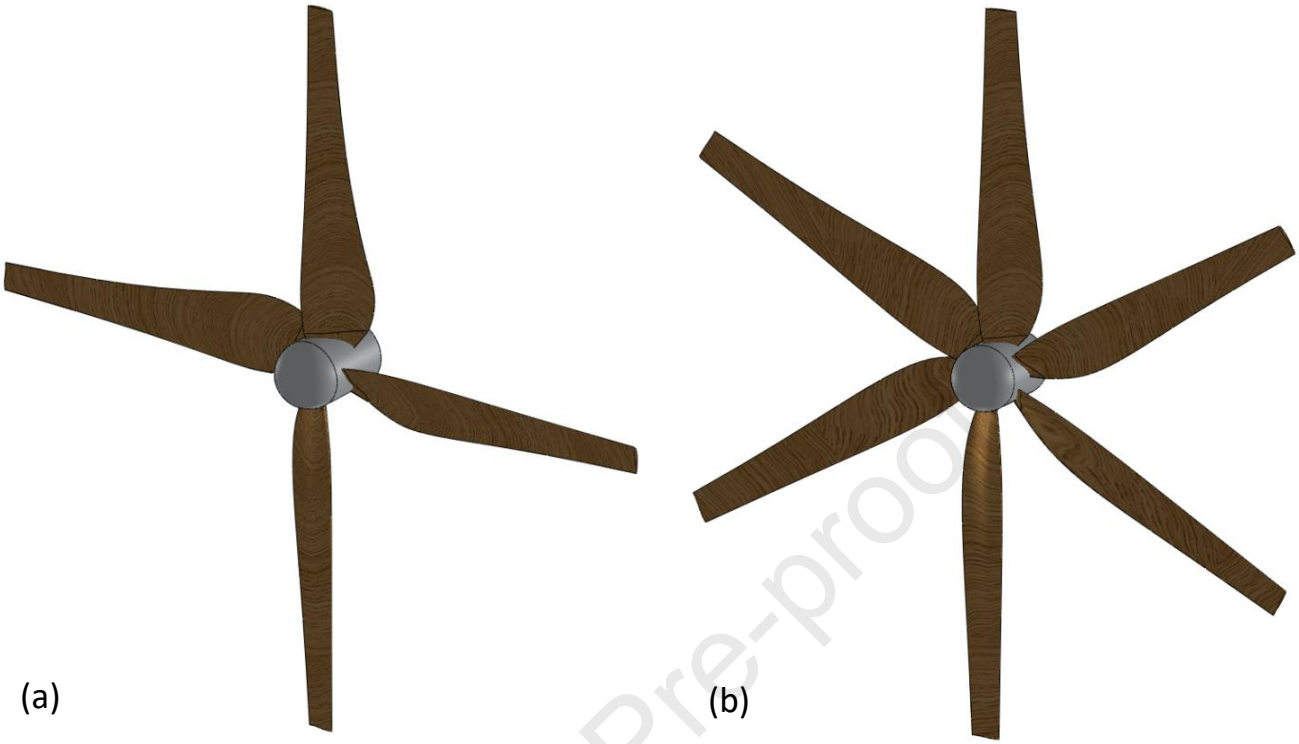

Fig. 26. The 0.9 m diameter *optimum* best C_P rotors (a) S826-TSR4-B4, and (b) S826-TSR3-B6.

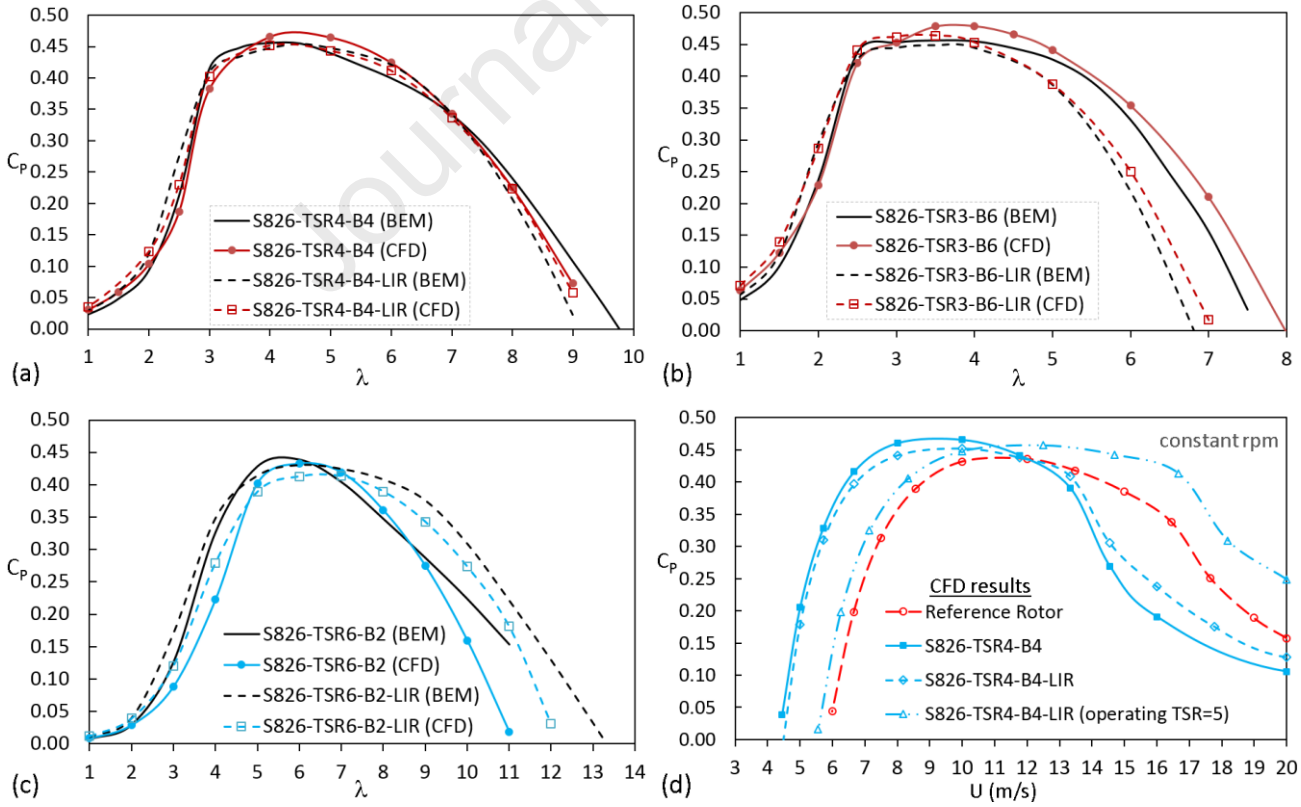

Fig. 27. BEM predictions with CFD results for (a, b) 0.9 m diameter optimum rotors and (c) S826-TSR6-B2. (d) C_P versus U for various S826-TSR4-B4 configurations compared to the Reference Rotor.

Multiple factors, such as low Reynolds number issues [89], finite blade number considerations [90], stall aerodynamics [55], rotational effects [91], three-dimensionality of the flow, and rotor wake turbulence, collectively limit the prediction capability of the BEM method.

Figure 28 displays the convergence history of the scaled residuals [71] and the torque for S826-TSR4-B4-LIR and S826-TSR6-B2-LIR at several λ values. When both the residuals and the torque value leveled off, the CFD runs were terminated. As seen, the torque consistently converged earlier than the residuals. In general, smaller residual values were attained with low-speed rotors. The residual values for stalled (lower than λ_{dsg}) and wake states (higher than λ_{dsg}) were larger than those for the optimum λ (λ_{dsg}) (Figures 28b and 28d).

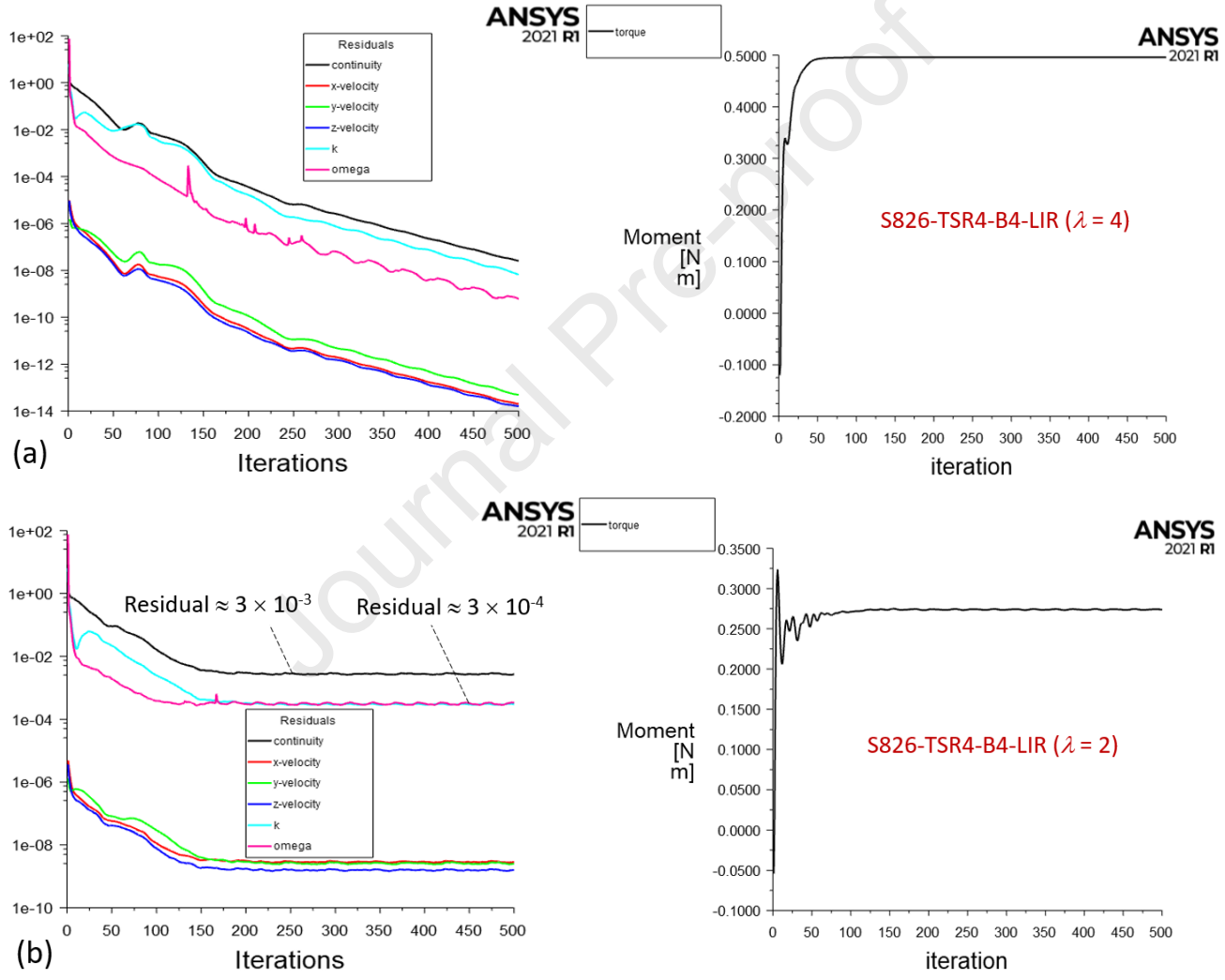

Fig. 28. (Continued) The convergence history of the scaled residuals and the torque acting on one blade.

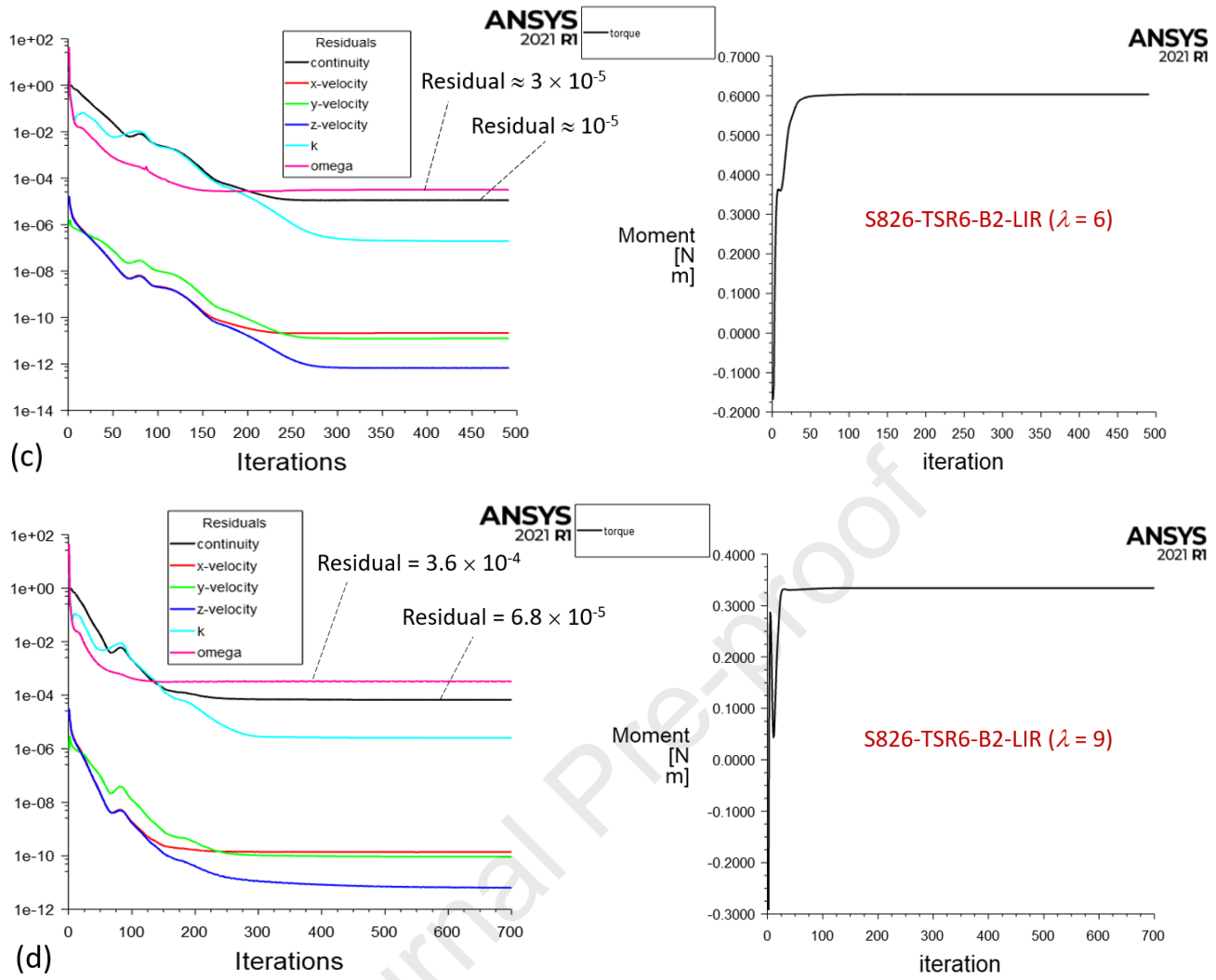

Fig. 28. The convergence history of the scaled residuals and the torque acting on one blade.

4 Conclusions

In the literature, multi-bladed rotors are often derived by adding or subtracting blades from the baseline rotor (usually three-bladed), in this manner, the optimum rotor solidity is searched. Although this approach produces higher C_P rotors compared to the 3-bladed rotor, it is unlikely to achieve the greatest C_P attainable for a multi-bladed rotor. It was found in the literature that the chord and pitch distributions optimized for maximum C_P tend to converge towards those of the Glauert optimum rotor. Therefore, in this work, the best C_P rotors were produced by scanning the design space of design TSR (λ_{dsg})-blade number using the Glauert optimum rotor design equations. The design lift coefficient was adapted to match the tip Reynolds number, rather than using a fixed value.

For rotor diameters of 0.9, 1.5, 2, and 3 m and blade number varying from 2 to 12, families of λ_{dsg}-$C_{P,max}$ curves were produced. The tip Reynolds number ranged from 0.5×10^5 to 6×10^5 for best C_P rotors. The 0.9, 1.5, 2 and

3 m diameter rotors with a design TSR of 4 achieved the greatest $C_{P,max}$ of 0.456, 0.483, 0.493, and 0.504, respectively, with 4, 6, 8, and 12 blades.

This research showed that adopting a low design TSR offers improvement in small wind turbine aerodynamic performance in a variety of ways. Low-speed rotors could provide the greatest $C_{P,max}$, high aerodynamic performance in off-design conditions, and high starting torque due to their inherent large blade pitch angles and solidity. This results in reduced starting time and wind speed, leading to extended operational time. High-speed rotors exhibit high C_P over a wider optimum TSR range, as confirmed by this research. Yet, this is an incomplete picture because TSR-C_P curves are typically produced for altering the rotor speed at a constant wind speed. The essential point is how the power coefficient changes with varying wind speed. This study shows that low TSR rotors experience a less deviation from the design TSR as wind speed varies. Consequently, low-speed rotors can effectively harness the turbulent wind while maintaining high C_P in comparison to high-speed rotors.

It is a common assumption that as the blade number increases, the rotor becomes bulkier. The rotational inertia of the Glauert optimum rotor increased with a decrease in design TSR and decreased with an increase in blade number due to thinner blades. As a result of these opposing effects, low-speed multi-blade best C_P rotors and high-speed 3-blade best C_P rotors exhibit a similar natural time constant, which is a measure of the rotors' ability to respond to wind speed changes.

Low induction rotors (LIRs), achieved by pitching the blades by 3 degrees, led to a small decrease in $C_{P,max}$, but significantly extended the optimum TSR and wind speed ranges for better aerodynamic efficiency. The λ_{dsg} threshold to expand the optimum wind speed range with the LIR option was 4, which coincided with the peak efficiency. When $\lambda_{dsg} < 4$, C_P decreased at low wind speeds, whereas the LIR option consistently raised C_P at high wind speeds, that carry more kinetic energy. When $\lambda_{dsg} < 3$, $C_{P,max}$ notably decreased, suggesting $\lambda_{dsg} = 3$ as the threshold for adopting the LIR option. Furthermore, a small rise in the rotor's operational TSR can effectively mitigate the off-design performance loss. This indicates that incorporating the low induction feature and optimizing rotor speed could enable the best C_P rotors to enhance the energy capture from the turbulent wind.

When compared to 3-blade high-speed rotors, low-speed low induction multi-blade rotors offered key advantages. According to the literature, increasing the blade pitch angles and chord towards the hub greatly improves starting features with minimal decrease in $C_{P,max}$. Starting wind speed was estimated to be about 2.5-3.5 m/s for 0.9 m and 1.5 m diameter low-speed best C_P rotors. These limiting speeds can be minimized by optimizing hub pitch and chord length for future work. As a final consideration, further investigations should consider dynamic BEM analyses or open-field experiments to assess the off-design performance of optimum rotors.

Appendix

The data presented in Fig. A1 was produced at a free wind speed of 10 m/s using the BEM algorithm, considering lift and drag coefficients depending on the local blade Reynolds number.

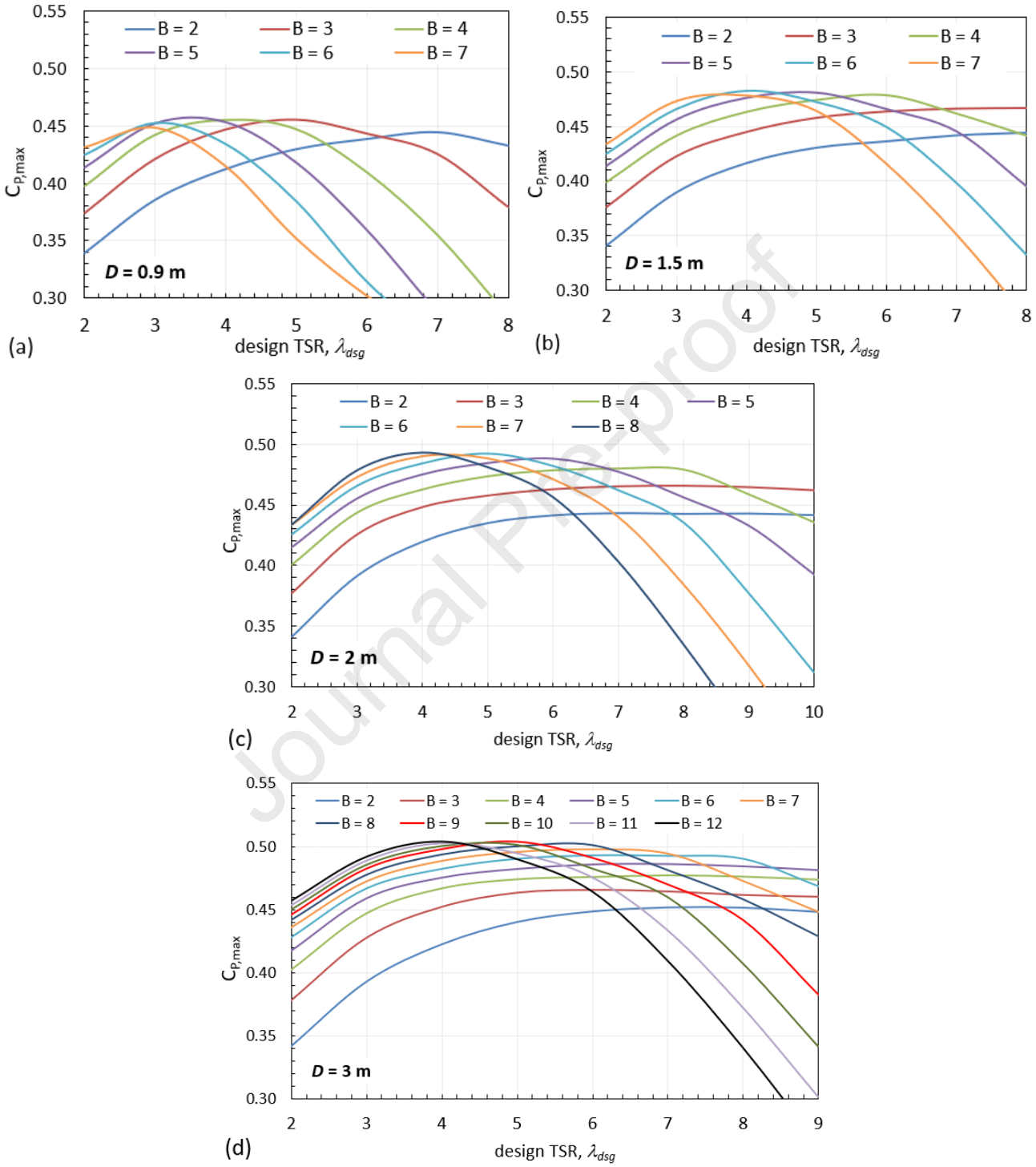

Fig. A1. The family of λ_{dsg}-$C_{P,\,max}$ curves for the best C_P S826 rotors with (a) 0.9 m, (b) 1.5 m, (c) 2 m, and (d) 3 m diameter.

Journal Pre-proof

Acknowledgements

The author would also like to appreciate Yildiz Technical University for the licence support of MATLAB and ANSYS FLUENT softwares.

References

[1] Global Wind Energy Council (GWEC). Global wind report 2022, https://gwec.net/global-wind-report-2022/; 2022 [accessed 8 February 2023]

[2] German Federal Ministry for Economic Affairs and Energy. Renewable energy sources in figures: National and international development 2021, https://www.bmwk.de/Redaktion/EN/Publikationen/Energie/renewable-energy-sources-in-figures-2020.html; 2021 [accessed 1 February 2023]

[3] Wood D. Small wind turbines: Analysis, design, and application. 1st ed. London: Springer; 2011.

[4] Chaudhary MK, Roy A. Design and optimization of a small wind turbine blade for operation at low wind speed. World J Eng 2015;12:83–94. https://doi.org/10.1260/1708-5284.12.1.83.

[5] TÜV Rheinland AG. Small Wind Turbines – The future of wind energy, https://www.tuv.com/content-media-files/master-content/global-landingpages/pdfs/e3/wind/tuv-rheinland-whitepaper_small_wind_energy_updated.pdf; 2015 [accessed 7 February 2023]

[6] Torres-Madroñero JL, Alvarez-Montoya J, Restrepo-Montoya D, Tamayo-Avendaño JM, Nieto-Londoño C, Sierra-Pérez J. Technological and operational aspects that limit small wind turbines performance. Energies 2020;13:1–40. https://doi.org/10.3390/en13226123.

[7] Distributed Wind Energy Association (DWEA). Is distributed wind right for me?, https://distributedwind.org/is-distributed-wind-right-for-me/; 2023 [accessed 15 May 2021]

[8] United States Department of Energy. Distributed wind market report 2022, https://www.energy.gov/eere/wind/articles/distributed-wind-market-report-2022-edition; 2022 [accessed 10 February 2023]

[9] Giguère P, Selig MS. Low Reynolds number airfoils for small horizontal axis wind turbines. Wind Eng 1997;21:367–80.

[10] Ge M, Tian D, Deng Y. Reynolds number effect on the optimization of a wind turbine blade for maximum aerodynamic efficiency. J Energy Eng 2016;142. https://doi.org/10.1061/(asce)ey.1943-7897.0000254.

[11] Yilmaz O. Increasing power coefficient of small wind turbine over a wide tip speed range by determining proper design tip speed ratio and number of blades. Proc Inst Mech Eng Part C J Mech Eng Sci 2022;236:11211–30. https://doi.org/10.1177/09544062221110396.

[12] Manwell JF, McGowan JG, Rogers AL. Wind energy explained. 3rd ed. Chichester: Wiley; 2009.

[13] Battisti L, Benini E, Brighenti A, Dell'Anna S, Raciti Castelli M. Small wind turbine effectiveness in the urban environment. Renew Energy 2018;129:102–13. https://doi.org/10.1016/j.renene.2018.05.062.

[14] Akbari V, Naghashzadegan M, Kouhikamali R, Afsharpanah F, Yaïci W. Multi-objective optimization and optimal airfoil blade selection for a small horizontal-axis wind turbine (HAWT) for application in regions with various wind potential. Machines 2022;10:687. https://doi.org/10.3390/machines10080687.

[15] Eco Power Shop Ltd. Rutland 1200 marine wind turbine, https://www.ecopowershop.com/rutland-1200-marine-wind-generator; 2023 [accessed 10 February 2023]

[16] Vaz JRP, Wood DH, Bhattacharjee D, Lins EF. Drivetrain resistance and starting performance of a small wind turbine. Renew Energy 2018;117:509–19. https://doi.org/10.1016/j.renene.2017.10.071.

[17] Worasinchai S, Ingram GL, Dominy RG. Effects of wind turbine starting capability on energy yield. J Eng Gas Turbines Power 2012;134:1–9. https://doi.org/10.1115/1.4004741.

[18] Pourrajabian A. Effect of blade profile on the external/internal geometry of a small horizontal axis wind turbine solid/hollow blade. Sustain Energy Technol Assessments 2022;51:101918. https://doi.org/10.1016/j.seta.2021.101918.

[19] Tang C, Soong WL, Freere P, Pathmanathan M, Ertugrul N. Dynamic wind turbine output power reduction under varying wind speed conditions due to inertia. Wind Energy 2013;16:561–73. https://doi.org/10.1002/we.1507.

[20] Pourrajabian A, Dehghan M, Javed A, Wood D. Choosing an appropriate timber for a small wind turbine blade: A comparative study. Renew Sustain Energy Rev 2019;100:1–8. https://doi.org/10.1016/j.rser.2018.10.010.

[21] Akour SN, Al-Heymari M, Ahmed T, Khalil KA. Experimental and theoretical investigation of micro wind turbine for low wind speed regions. Renew Energy 2018;116:215–23. https://doi.org/10.1016/j.renene.2017.09.076.

[22] Yang Z, Yin M, Xu Y, Zou Y, Dong Z, Zhou Q. Inverse aerodynamic optimization considering impacts of design tip speed ratio for variable-speed wind turbines. Energies 2016;9:1023. https://doi.org/10.3390/en9121023.

[23] Singh RK, Ahmed MR. Blade design and performance testing of a small wind turbine rotor for low wind speed applications. Renew Energy 2013;50:812–9. https://doi.org/10.1016/j.renene.2012.08.021.

[24] Zhang T, Wang Z, Huang W, Ingham D, Ma L, Pourkashanian M. A numerical study on choosing the best configuration of the blade for vertical axis wind turbines. J Wind Eng Ind Aerodyn 2020;201:104162. https://doi.org/10.1016/j.jweia.2020.104162.

[25] Pagnini LC, Burlando M, Repetto MP. Experimental power curve of small-size wind turbines in turbulent urban environment. Appl Energy 2015;154:112–21. https://doi.org/10.1016/j.apenergy.2015.04.117.

[26] Zhang T tian, Elsakka M, Huang W, Wang Z guo, Ingham DB, Ma L, et al. Winglet design for vertical axis wind turbines based on a design of experiment and CFD approach. Energy Convers Manag 2019;195:712–26. https://doi.org/10.1016/j.enconman.2019.05.055.

[27] Kanya B, Visser K. The impact of airfoil selection on the design of small horizontal axis wind turbines. 48th AIAA Aerospace Sciences Meeting Including the New Horizons Forum and Aerospace Exposition. Orlando, Florida, USA, 4-7 January 2010.

[28] Scappatici L, Bartolini N, Castellani F, Astolfi D, Garinei A, Pennicchi M. Optimizing the design of horizontal-axis small wind turbines: From the laboratory to market. J Wind Eng Ind Aerodyn 2016;154:58–68. https://doi.org/10.1016/j.jweia.2016.04.006.

[29] Eltayesh A, Castellani F, Burlando M, Bassily Hanna M, Huzayyin AS, El-Batsh HM, et al. Experimental and numerical investigation of the effect of blade number on the aerodynamic performance of a small-scale horizontal axis wind turbine. Alexandria Eng J 2021;60:3931–44. https://doi.org/10.1016/j.aej.2021.02.048.

[30] Porto HA, Fortulan CA, Porto AJV. Power performance of starting-improved and multi-bladed horizontal-axis small wind turbines. Sustain Energy Technol Assessments 2022;53:102341. https://doi.org/10.1016/j.seta.2022.102341.

[31] Vedovelli M, Eltayesh A, Natili F, Castellani F. Experimental and numerical investigation of the effect of blades number on the dynamic response of a small horizontal-axis wind turbine. Energies 2022;15:9134. https://doi.org/10.3390/en15239134.

[32] Visser KD. Wind tamer turbine performance report. New York: Department of Mechanical and Aeronautical Engineering, Clarkson University; 2009.

[33] Sessarego M, Wood D. Multi-dimensional optimization of small wind turbine blades. Renewables Wind Water, Sol 2015;2:9. https://doi.org/10.1186/s40807-015-0009-x.

[34] Pinto RLU de F, Gonçalves BPF. A revised theoretical analysis of aerodynamic optimization of horizontal-axis wind turbines based on BEM theory. Renew Energy 2017;105:625–36. https://doi.org/10.1016/j.renene.2016.12.076.

[35] Pourrajabian A, Afshar PAN, Mirzaei M, Ebrahimi R, Wood DH. Hollow blades for small wind turbines operating at high altitudes. J Sol Energy Eng 2016;138:1–8. https://doi.org/10.1115/1.4034333.

[36] Bottasso CL, Croce A, Sartori L. Free-form design of low induction rotors. 33rd Wind Energy Symposium (AIAA), Kissimmee, Florida, USA, 5-9 January 2015.

[37] Ribnitzky D, Berger F, Kühn M. Innovative aerodynamic rotor concept for demand-oriented power feed-in of offshore wind turbines. J Phys Conf Ser 2022;2265:032017. https://doi.org/10.1088/1742-6596/2265/3/032017.

[38] Jamieson P. Top-level rotor optimisations based on actuator disc theory. Wind Energy Sci 2020;5:807–18. https://doi.org/10.5194/wes-5-807-2020.

[39] Bortolotti P, Bottasso CL, Croce A. Combined preliminary-detailed design of wind turbines. Wind Energy Sci 2016;1:71–88. https://doi.org/10.5194/wes-1-71-2016.

[40] Sant T, Farrugia RN, Muscat M, Caruana C, Axisa R, Borg A, et al. Development and performance testing of a small, multi-bladed wind turbine. Wind Eng 2020;44:3–20. https://doi.org/10.1177/0309524X19849845.

[41] Kaya MN, Uzol O, Ingham D, Köse F, Buyukzeren R. The aerodynamic effects of blade pitch angle on small horizontal axis wind turbines. Int J Numer Methods Heat Fluid Flow 2023;33:120–34. https://doi.org/10.1108/HFF-02-2022-0128.

[42] Rocha PAC, Carneiro de Araujo JW, Lima RJP, Vieira da Silva ME, Albiero D, de Andrade CF, et al. The effects of blade pitch angle on the performance of small-scale wind turbine in urban environments. Energy 2018;148:169–78. https://doi.org/10.1016/j.energy.2018.01.096.

[43] Wilson RE, Lissaman PBS, Walker SN. Aerodynamic performance of wind turbines. Oregon, USA: Department of Mechanical Engineering, Oregon State University; 1976.

[44] Bourhis M, Pereira M, Ravelet F, Dobrev I. Innovative design method and experimental investigation of a small-scale and very low tip-speed ratio wind turbine. Exp Therm Fluid Sci 2022;130:110504. https://doi.org/10.1016/j.expthermflusci.2021.110504.

[45] Bourhis M, Pereira M, Ravelet F. Experimental investigation of the effect of blade solidity on micro-

scale and low tip-speed ratio wind turbines. Exp Therm Fluid Sci 2022;140:110745. https://doi.org/10.1016/j.expthermflusci.2022.110745.

[46] Sarkis N, Pinilla AE. Experimental study on a model of a commercial windpumping rotor. Wind Eng 2006;30:511–20. https://doi.org/10.1260/030952406779994178.

[47] John IH, Wood DH, Vaz JRP. Helical vortex theory and blade element analysis of multi-bladed windmills. Wind Energy 2023;26:228–46. https://doi.org/10.1002/we.2796.

[48] Zhang H, Wen J, Zhan J, Xin D. Effects of blade number on the aerodynamic performance and wake characteristics of a small horizontal-axis wind turbine. Energy Convers Manag 2022;273:116410. https://doi.org/10.1016/j.enconman.2022.116410.

[49] Duquette MM, Swanson J, Visser KD. Solidity and blade number effects on a fixed pitch, 50 W horizontal axis wind turbine. Wind Eng 2003;27:299–316. https://doi.org/10.1260/030952403322665271.

[50] Brasil Junior ACP, Mendes RCF, Wirrig T, Noguera R, Oliveira TF. On the design of propeller hydrokinetic turbines: The effect of the number of blades. J Brazilian Soc Mech Sci Eng 2019;41:1–14. https://doi.org/10.1007/s40430-019-1753-4.

[51] Bourhis M, Pereira M, Ravelet F. Performance and flow characteristics of the optimum rotors of Betz, Joukowsky, and Glauert at low tip-speed ratio. Phys Fluids 2022;34:105105. https://doi.org/10.1063/5.0107962.

[52] Song Q, Lubitz WD. BEM simulation and performance analysis of a small wind turbine rotor. Wind Eng 2013;37:381–99. https://doi.org/10.1260/0309-524X.37.4.381.

[53] Buhl ML. A new empirical relationship between thrust coefficient and induction factor for the turbulent windmill state. Colorado, USA: National Renewable Energy Laboratory, Report no: NREL/TP-500-36834; 2005.

[54] Refan M, Hangan H. Aerodynamic performance of a small horizontal axis wind turbine. J Sol Energy Eng Trans ASME 2012;134:1–7. https://doi.org/10.1115/1.4005751.

[55] Lanzafame R, Messina M. Fluid dynamics wind turbine design: Critical analysis, optimization and application of BEM theory. Renew Energy 2007;32:2291–305. https://doi.org/10.1016/j.renene.2006.12.010.

[56] Bartl J, Sagmo KF, Bracchi T, Sætran L. Performance of the NREL S826 airfoil at low to moderate Reynolds numbers—A reference experiment for CFD models. Eur J Mech B/Fluids 2019;75:180–92. https://doi.org/10.1016/j.euromechflu.2018.10.002.

[57] Song Q. Design, fabrication, and testing of a new small wind turbine blade. Ontario, Canada: Master's thesis, University of Guelph; 2012.

[58] Krogstad P-Å, Lund JA. An experimental and numerical study of the performance of a model turbine. Wind Energy 2012;15:443–57. https://doi.org/10.1002/we.482.

[59] Somers D. The S825 and S826 airfoils. Colorado, USA: National Renewable Energy Laboratory, Report no:NREL/SR-500-36344; 2005.

[60] Bahaj AS, Molland AF, Chaplin JR, Batten WMJ. Power and thrust measurements of marine current turbines under various hydrodynamic flow conditions in a cavitation tunnel and a towing tank. Renew Energy 2007;32:407–26. https://doi.org/10.1016/j.renene.2006.01.012.

[61] Dogru S. Aerodynamic optimization of diffuser for horizontal axis wind turbine. Istanbul, Turkey: Master's thesis, Yildiz Technical University; 2019.

[62] Abdelrahman MA, Abdellatif OE, Moawed M, Eliwa A, Misak S. The CFD performance analysis for horizontal axis wind turbine with different blade shapes and tower effect. 2015 16th International Scientific Conference on Electric Power Engineering (IEEE), Kouty nad Desnou, Czech Republic, 20-22 May 2015.

[63] Martínez J, Bernabini L, Probst O, Rodríguez C. An improved BEM model for the power curve prediction of stall-regulated wind turbines. Wind Energy 2005;8:385–402. https://doi.org/10.1002/we.147.

[64] Pourrajabian A, Nazmi Afshar PA, Ahmadizadeh M, Wood D. Aero-structural design and optimization of a small wind turbine blade. Renew Energy 2016;87:837–48. https://doi.org/10.1016/j.renene.2015.09.002.

[65] Verma N, Baloni BD. Influence of Reynolds number consideration for aerodynamic characteristics of airfoil on the blade design of small horizontal axis wind turbine. Int J Green Energy 2022;19:733–46. https://doi.org/10.1080/15435075.2021.1960356.

[66] Peterson P, Clausen PD. Timber for high efficiency small wind turbine blades. Wind Eng 2004;28:87–96. https://doi.org/10.1260/0309524041210865.

[67] Tangler JL. The evolution of rotor and blade design. Colorado, USA: National Renewable Energy Laboratory, Report no: NREL/CP-500-28410; 2000.

[68] Wright AK, Wood DH. The starting and low wind speed behaviour of a small horizontal axis wind turbine. J Wind Eng Ind Aerodyn 2004;92:1265–79. https://doi.org/10.1016/j.jweia.2004.08.003.

[69] Kreyszig E. Advanced engineering mathematics. 10th ed. New Jersey: John Wiley & Sons; 2011.

[70] Silva PASF, Rio Vaz DATD, Britto V, de Oliveira TF, Vaz JRP, Brasil Junior ACP. A new approach for the design of diffuser-augmented hydro turbines using the blade element momentum. Energy Convers Manag 2018;165:801–14. https://doi.org/10.1016/j.enconman.2018.03.093.

[71] ANSYS Inc. Ansys fluent theory guide Canonsburg, PA: ANSYS, Inc. 2021.

[72] Ou M, Yan L, Huang W, Li S bin, Li L quan. Detailed parametric investigations on drag and heat flux reduction induced by a combinational spike and opposing jet concept in hypersonic flows. Int J Heat Mass Transf 2018;126:10–31. https://doi.org/10.1016/j.ijheatmasstransfer.2018.05.013.

[73] Elfarra MA, Sezer Uzol N, Akmandor IS. Investigations on blade tip tilting for HAWT rotor blades using CFD. Int J Green Energy 2015;12:125–38. https://doi.org/10.1080/15435075.2014.889007.

[74] Spalart P, Allmaras S. A one-equation turbulence model for aerodynamic flows. 30th AIAA Aerospace Sciences Meeting and Exhibit, Reno, Nevada, USA, 6-9 January 1992.

[75] Aranake AC, Lakshminarayan VK, Duraisamy K. Computational analysis of shrouded wind turbine configurations using a 3-dimensional RANS solver. Renew Energy 2015;75:818–32. https://doi.org/10.1016/j.renene.2014.10.049.

[76] Sagol E, Reggio M, Ilinca A, Sahin AZ, Yu B. Assessment of two-equation turbulence models and validation of the performance characteristics of an experimental wind turbine by CFD. Int Sch Res Netw ISRN Mech Eng 2012;2012:1-10. https://doi.org/10.5402/2012/428671.

[77] S. A. Orszag, V. Yakhot, W. S. Flannery, F. Boysan, D. Choudhury, J. Maruzewski and BP. Renormalization group modeling and turbulence simulations. International Conference on Near-Wall Turbulent Flows, Tempe, Arizona, 1993.

[78] Rezaeiha A, Montazeri H, Blocken B. On the accuracy of turbulence models for CFD simulations of vertical axis wind turbines. Energy 2019;180:838–57. https://doi.org/10.1016/j.energy.2019.05.053.

[79] Menter FR. Two-equation eddy-viscosity turbulence models for engineering applications. AIAA J 1994;32:1598–605. https://doi.org/10.2514/3.12149.

[80] Zhang R rui, Huang W, Li L quan, Yan L, Moradi R. Drag and heat flux reduction induced by the pulsed counterflowing jet with different periods on a blunt body in supersonic flows. Int J Heat Mass Transf 2018;127:503–12. https://doi.org/10.1016/j.ijheatmasstransfer.2018.08.066.

[81] Johansen J, Madsen HA, Gaunaa M, Bak C, Srensen NN. Design of a wind turbine rotor for maximum aerodynamic efficiency. Wind Energy 2009;12:261–73. https://doi.org/10.1002/we.292.

[82] Khalafallah MG, Ahmed AM, Emam MK. CFD study of some factors affecting performance of HAWT with swept blades. Int J Sustain Energy 2017;36:489–501. https://doi.org/10.1080/14786451.2015.1053394.

[83] Hsiao F Bin, Bai CJ, Chong WT. The performance test of three different horizontal axis wind turbine (HAWT) blade shapes using experimental and numerical methods. Energies 2013;6:2784–803. https://doi.org/10.3390/en6062784.

[84] Sørensen NN, Michelsen JA, Schreck S. Navier-Stokes predictions of the NREL phase VI rotor in the NASA Ames 80 ft × 120 ft wind tunnel. Wind Energy 2002;5:151–69. https://doi.org/10.1002/we.64.

[85] Lanzafame R, Mauro S, Messina M. Wind turbine CFD modeling using a correlation-based transitional model. Renew Energy 2013;52:31–9. https://doi.org/10.1016/j.renene.2012.10.007.

[86] Jamieson P. Generalized limits for energy extraction in a linear constant velocity flow field. Wind Energy 2008;11:445–57. https://doi.org/10.1002/we.268.

[87] Jamieson PM. Beating betz: Energy extraction limits in a constrained flow field. J Sol Energy Eng Trans ASME 2009;131:0310081–6. https://doi.org/10.1115/1.3139143.

[88] Jamieson P. Innovation in wind turbine design. 1st ed. New Jersey: John Wiley & Sons; 2011.

[89] Genc MS. Low Reynolds number aerodynamics and transition. 1st ed. Rijeka: InTech; 2012.

[90] Vaz JRP, Okulov VL, Wood DH. Finite blade functions and blade element optimization for diffuser-augmented wind turbines. Renew Energy 2021;165:812–22. https://doi.org/10.1016/j.renene.2020.11.059.

[91] Sicot C, Devinant P, Loyer S, Hureau J. Rotational and turbulence effects on a wind turbine blade. Investigation of the stall mechanisms. J Wind Eng Ind Aerodyn 2008;96:1320–31. https://doi.org/10.1016/j.jweia.2008.01.013.

Journal Pre-proof

Journal Pre-proof

Highlights

- Operating TSR of low-speed rotor deviates less from design TSR as wind speed varies
- Low induction rotor expands optimum TSR and wind speed range for high efficiency
- Low-speed multi-blade rotors achieve high $C_{P,max}$, better efficiency at off-design
- Multi-blade best C_P rotors have about same natural time as 3-blade best C_P rotors
- Scanning design TSR-blade number for 0.9, 1.5, 2, and 3 m diameter S826 rotors

Journal Pre-proof

Journal Pre-proof

Declaration of interests

☒ The authors declare that they have no known competing financial interests or personal relationships that could have appeared to influence the work reported in this paper.

☐ The authors declare the following financial interests/personal relationships which may be considered as potential competing interests:

Journal Pre-proof